

**Title:** Stable Pom1 clusters form a glucose-modulated concentration gradient that regulates mitotic entry

**Authors:** Corey A.H. Allard, Hannah E. Opalko, and James B. Moseley\*

**Author Affiliations:** Department of Biochemistry and Cell Biology  
The Geisel School of Medicine at Dartmouth, Hanover, NH 03755

\*Corresponding author

[james.b.moseley@dartmouth.edu](mailto:james.b.moseley@dartmouth.edu)

**Abstract:** Control of cell size requires molecular size sensors that are coupled to the cell cycle. Rod-shaped fission yeast cells divide at a threshold size partly due to Cdr2 kinase, which forms nodes at the medial cell cortex where it inhibits the Cdk1-inhibitor Wee1. Pom1 kinase phosphorylates and inhibits Cdr2, and forms cortical concentration gradients from cell poles. Pom1 inhibits Cdr2 signaling to Wee1 specifically in small cells, but the time and place of their regulatory interactions were unclear. We show that Pom1 forms stable oligomeric puncta that dynamically sample the cell cortex. Binding frequency is patterned into a concentration gradient by the polarity landmarks Tea1 and Tea4. Pom1 puncta colocalize with Cdr2 nodes, forming a glucose-modulated inhibitory threshold against node activation. Our work reveals how Pom1-Cdr2-Wee1 operates in multiprotein clusters at the cell cortex to promote mitotic entry at a specific size that can be modified by nutrient availability.

## 1 **Introduction:**

2 Many cell types display a remarkable ability to maintain a constant size during  
3 rapid cycles of growth and division ([Fantes and Nurse, 1977](#); [Ginzberg et al., 2015](#);  
4 [Jorgensen and Tyers, 2004](#); [Lloyd, 2013](#)). Such cell size control is a systems-level  
5 property that emerges from the integration of multiple size-dependent signal transduction  
6 pathways. Each signaling pathway is comprised of tunable biochemical parameters,  
7 including gene-expression and post-translational modifications such as protein  
8 phosphorylation ([Alberghina et al., 2009](#)). One major challenge in cell size research is to  
9 understand the biochemical mechanisms of signal transduction in each pathway, and  
10 what makes them size-dependent. These control systems can generate size homogeneity  
11 for a given cell type, but cell size is also an adaptable property. For example, nutritional  
12 cues and other environmental factors can alter cell size ([Fantes and Nurse, 1977](#); [Kelkar  
13 and Martin, 2015](#); [Shiozaki, 2009](#); [Yanagida Mitsuhiro et al., 2011](#)). Thus, a second major  
14 challenge in cell size research is to understand how size-dependent signaling pathways  
15 respond to changes in cell metabolism and stress.

16  
17 In eukaryotic cells, these signaling pathways lead to regulated activation of the  
18 conserved cyclin-dependent kinase Cdk1 ([Harashima et al., 2013](#)). Activated Cdk1  
19 triggers mitotic entry and the cascade of events that lead to cell division ([Gould and Nurse,  
20 1989](#); [Simanis and Nurse, 1986](#)). The fission yeast *Schizosaccharomyces pombe*  
21 represents an excellent model system to study size-dependent signaling pathways that  
22 regulate Cdk1. Genetic screens performed in past decades have identified many  
23 conserved factors that regulate Cdk1, but how these factors form size-dependent  
24 signaling pathways remains less clear. Fission yeast cells have a simple geometry that  
25 facilitates cell size studies. These cylindrical cells maintain a constant cell width, and grow  
26 by linear extension during interphase ([Fantes and Nurse, 1977](#); [Moreno et al., 1989](#)). A  
27 network of cell polarity proteins positioned at cell tips restricts growth to these sites and  
28 maintains proper cell morphology ([Chang and Martin, 2009](#)). As a result, cell length  
29 doubles in one cell cycle, and many aspects of cell geometry scale with this increase in  
30 cell length ([Gu and Oliferenko, 2019](#); [Neumann and Nurse, 2007](#)). Recent studies used  
31 cell shape mutants to show that fission yeast cells primarily measure surface area, not

32 length or volume, for cell size control (Facchetti et al., 2019; Pan et al., 2014). A critical  
33 next step is to understand how signaling pathways that regulate Cdk1 might operate at  
34 the cell cortex in a size-dependent manner.

35  
36 In all eukaryotes, Cdk1 activity is established by the opposing activities of the  
37 inhibitory protein kinase Wee1, and the counteracting phosphatase Cdc25 (Gautier et al.,  
38 1991; Gould and Nurse, 1989; Kumagai and Dunphy, 1991; Russell and Nurse, 1986,  
39 1987; Strausfeld et al., 1991). In fission yeast, mutations in Wee1, Cdc25, and their  
40 upstream regulators lead to changes in cell size that correspond to changes in the  
41 signaling pathways. Separate mechanisms appear to link cell size with regulation of Wee1  
42 versus Cdc25. For Cdc25, its cellular concentration increases through unknown  
43 mechanisms as cells grow during interphase (Keifenheim et al., 2017; Moreno et al.,  
44 1990). In contrast, the concentration of Wee1 remains constant during interphase, but it  
45 is progressively phosphorylated by the conserved inhibitory kinases Cdr1 and Cdr2  
46 (Aligue et al., 1997; Breeding et al., 1998; Kanoh and Russell, 1998; Keifenheim et al.,  
47 2017; Lucena et al., 2017; Opalko and Moseley, 2017; Russell and Nurse, 1987; Wu and  
48 Russell, 1993; Young and Fantes, 1987). *cdr2* mutants fail to divide at a constant surface  
49 area, and instead dividing according to cell volume or length (Facchetti et al., 2019). This  
50 change suggests that Cdr2-Cdr1-Wee1 signaling underlies the primary size-sensing  
51 pathway that relates to surface area, while additional pathways related to volume and  
52 length are engaged in its absence. The localization of Cdr2, Cdr1, and Wee1 supports  
53 this model. Cdr2 forms punctate oligomeric structures called nodes that stably bind to the  
54 medial cell cortex, and recruits Cdr1 to these sites (Akamatsu et al., 2014, 2017; Guzmán-  
55 Vendrell et al., 2015; Martin and Berthelot-Grosjean, 2009; Morrell et al., 2004; Moseley  
56 et al., 2009). Wee1 localizes primarily in the nucleus and spindle-pole body, where it  
57 encounters Cdk1 to prevent mitotic entry (Masuda et al., 2011; Moseley et al., 2009; Wu  
58 et al., 1996). In addition, Wee1 transiently visits cortical Cdr1/2 nodes in bursts that lead  
59 to inhibition of Wee1 kinase activity (Allard et al., 2018). The frequency and duration of  
60 these Wee1 bursts at Cdr1/2 nodes increase approximately twenty-fold as cells double in  
61 size during interphase (Allard et al., 2018). This mechanism leads to size-dependent  
62 inhibition of Wee1 by a signaling pathway at the cell surface.

63  
64       This size-dependent change in Wee1 bursting dynamics is encoded into the Cdr1-  
65 Cdr2-Wee1 pathway at two proposed levels. First, increased Wee1 bursting depends  
66 upon the doubling in number of Cdr1/2 nodes, which occurs as growth results in a  
67 doubling of cell surface area, but this increase is smaller than the magnitude of change  
68 in Wee1 bursting (~2-fold vs ~20-fold) (Allard et al., 2018; Deng and Moseley, 2013; Pan  
69 et al., 2014). Second, activation of Cdr2 increases as cells increase in size (Deng et al.,  
70 2014). Cdr2 kinase activity is required for Wee1 localization to nodes, and is controlled  
71 by the upstream kinase Pom1 (Allard et al., 2018; Moseley et al., 2009). Pom1 directly  
72 phosphorylates and inhibits the activation of Cdr2 (Bhatia et al., 2014; Deng et al., 2014;  
73 Kettenbach et al., 2015; Martin and Berthelot-Grosjean, 2009; Moseley et al., 2009).  
74 Pom1 also phosphorylates a separate set of sites on Cdr2 to disrupt oligomerization and  
75 membrane binding (Bhatia et al., 2014; Rincon et al., 2014). This regulation of Cdr2 by  
76 Pom1 changes the size dependency of Wee1 bursts. Specifically, the frequency and  
77 duration of Wee1 bursts at Cdr1/2 nodes increases, but only in small cells (Allard et al.,  
78 2018). Consistent with this defect, *pom1* $\Delta$  cells divide at a small size due to dysregulation  
79 of the Cdr2-Cdr1-Wee1 pathway (Bähler and Pringle, 1998; Bhatia et al., 2014; Martin  
80 and Berthelot-Grosjean, 2009; Moseley et al., 2009; Wood and Nurse, 2013). Taken  
81 together, these results suggest a size-dependent interaction between Pom1 and its  
82 substrate Cdr2. However, the location and timing of Pom1 interactions with Cdr2 have  
83 remained poorly defined.

84  
85       Pom1 localizes in a spatial gradient that is enriched at cell tips, with a lower  
86 concentration at the medial cell cortex, where its substrate Cdr2 forms nodes (Bähler and  
87 Pringle, 1998; Bhatia et al., 2014; Martin and Berthelot-Grosjean, 2009; Moseley et al.,  
88 2009; Pan et al., 2014). Thus, the majority of Pom1 and Cdr2 molecules in a cell are  
89 spatially separated, raising the question of when and where they interact. Several lines  
90 of evidence suggest that the spatial distributions of Pom1 and Cdr2 are critical for the  
91 size-dependent signaling properties of this pathway, and suggest the lateral cell cortex  
92 as the key interface. For example, ectopic targeting of Pom1 to the medial cell cortex  
93 inhibits Cdr2 node formation and Cdr2-dependent cell size signaling (Martin and

94 [Berthelot-Grosjean, 2009](#)). Additionally, the Pom1 gradient is dissipated as part of a  
95 cellular response to glucose deprivation, which leads to increased Pom1 concentration at  
96 the lateral cortex where it delays mitotic entry ([Kelkar and Martin, 2015](#)). This result also  
97 demonstrates that Pom1-Cdr2 signaling responds to environmental input to coordinate  
98 cell size with nutrient availability. In this system, Pom1 functions analogously to an  
99 intracellular morphogen, acting as a concentration-dependent and localization-controlled  
100 inhibitor of Cdr2 nodes. However, levels of Pom1 at the medial cell cortex in wild-type  
101 cells growing under steady state conditions are low, constant, and do not vary with cell  
102 size ([Bhatia et al., 2014](#); [Pan et al., 2014](#)). The mechanism by which Pom1 provides size  
103 specific input to Cdr2 is unclear and requires analysis of their molecular dynamics at the  
104 lateral cell cortex.

105  
106 Past studies have led to a model for Pom1 gradient formation driven by the binding  
107 and diffusion of individual Pom1 molecules in the plasma membrane ([Hachet et al., 2011](#);  
108 [Saunders et al., 2012](#)). Pom1 binds directly to anionic phospholipids at the cell cortex,  
109 and these interactions are disrupted upon intramolecular autophosphorylation ([Hachet et](#)  
110 [al., 2011](#)). Polarity factors including Tea1 and Tea4 are enriched at the cell tips by  
111 microtubules, where they recruit the protein phosphatase 1 (PP1) Dis2, which  
112 dephosphorylates Pom1 to promote membrane attachment specifically at the cell tip  
113 ([Hachet et al., 2011](#)). Cortical Pom1 molecules are then thought to diffuse in the plane of  
114 the membrane away from the tip, until multiple autophosphorylation events disrupt  
115 membrane binding ([Hachet et al., 2011](#); [Hersch et al., 2015](#); [Saunders et al., 2012](#)). Tip-  
116 concentrated Pom1 occludes Cdr1/2 node formation, restricting them instead to the  
117 medial cell cortex ([Martin and Berthelot-Grosjean, 2009](#); [Moseley et al., 2009](#)).  
118 Intriguingly, dynamic clusters of Pom1 have also been observed and are proposed to form  
119 by unstable oligomerization of molecules diffusing in the plane of the membrane ([Hachet](#)  
120 [et al., 2011](#); [Saunders et al., 2012](#)). These clusters are thought to form and decay rapidly,  
121 temporarily sequestering Pom1 molecules and thereby slowing molecular diffusion rates  
122 and reducing noise in the gradient ([Saunders et al., 2012](#)). These puncta represent nano-  
123 scale pockets of increased Pom1 concentration, but whether these clusters contribute to  
124 regulation of Cdr2 nodes is unknown.

125  
126 Here, we use biochemical approaches in combination with quantitative TIRF and  
127 confocal microscopy to show that the Pom1 gradient itself is formed by these punctate  
128 clusters. Pom1 puncta are stable oligomers that bind and release the membrane with  
129 minimal lateral diffusion. The frequency of Pom1 puncta binding is higher at cell tips than  
130 on cell sides. Thus, the gradient is formed because the membrane-association frequency  
131 of Pom1 puncta is patterned along the long axis of the cell. A portion of Pom1 puncta in  
132 the medial cell cortex colocalize with Cdr2 nodes, and the ratio of Pom1 to Cdr2 at the  
133 medial cell cortex changes as a function of cell size. When glucose availability is  
134 restricted, Pom1 clusters redistribute to the medial cell cortex to prevent dramatic  
135 dysregulation of Wee1 bursts. Our work reveals that the Pom1-Cdr2-Wee1 signaling  
136 pathway is organized as a series of cortical clusters. The relative distribution of these  
137 clusters at the plasma membrane changes with cell size and glucose availability, thus  
138 relaying cell surface area to the core cell cycle machinery in a nutrient-controlled manner.  
139

## 140 **Results:**

### 141 **The Pom1 gradient is formed by transient cortical puncta**

142 We sought to examine the molecular dynamics of Pom1-Cdr2 signaling at the cell  
143 cortex. As a starting point, we imaged Pom1 by TIRF microscopy, which selectively  
144 excites fluorophores near the coverslip. Pom1 was tagged at the endogenous locus with  
145 the bright and photostable fluorophore mNeonGreen (mNG). Surprisingly, along the  
146 lateral cell cortex Pom1-mNG was localized almost exclusively in discreet puncta, with no  
147 apparent diffuse signal (**Figure 1A**). In images from a single time-point, Pom1 puncta  
148 formed a noisy concentration gradient (**Figure 1B**). Time-averaging produced a smoother  
149 gradient dotted by occasional clusters, similar to the gradient observed by confocal  
150 microscopy (**Figure 1A-B**). Similar results were obtained by confocal microscopy (**Figure**  
151 **S1A-H**). Pom1 puncta were highly dynamic. They appeared on the lateral cortex with a  
152 frequency of  $\sim 2 \text{ puncta} \cdot \mu\text{m}^{-2} \cdot \text{s}^{-1}$ , and remained bound for less than 2 seconds on average  
153 (**Figure 1C,F,H**). During this brief cortical attachment, Pom1 puncta exhibited minimal  
154 diffusion which lacked directionality, and instead appeared to diffuse randomly in sub-  
155 micron patches of cortex (**Figure 1C,G**).

156  
157 Similar puncta were previously observed by confocal microscopy, but they were  
158 not thought to form the Pom1 concentration gradient *per se* (Hachet et al., 2011;  
159 Saunders et al., 2012). Our findings suggested the distinct possibility that the cortical  
160 gradient itself is comprised of dynamic puncta. To test this possibility, we needed to image  
161 Pom1-mNG at cell tips, which are inaccessible to visualization using standard slide  
162 preparation for TIRF microscopy because this region is outside of the TIRF illumination  
163 field. Therefore, we performed “head-on” TIRF imaging of cell tips. Pom1-mNG localized  
164 at cell tips almost entirely in puncta, similar to cell sides (Figure 1D-E). We also used  
165 “head-on” Airyscan confocal imaging to confirm that Pom1 localization in puncta at tips  
166 was not an artifact of the TIRF approach (Figure S1I), a conclusion also supported by  
167 work using high resolution wide-field microscopy (Dodgson et al., 2013). Compared to  
168 cell sides, Pom1 puncta appeared twice as frequently at cell tips but with a similar cortical  
169 duration, again exhibiting minimal and non-directional diffusion away from their binding  
170 site (Figure 1F-H). Fluorescence intensity of individual puncta at cell tips and cell sides  
171 were similar, although we detected a low number of brighter puncta at cell tips, likely  
172 representing multiple diffraction-limited puncta (Figure 1I, Figure S1I-K). From these  
173 data, we conclude that the Pom1 gradient is formed by patterning the membrane binding  
174 frequency of cortical puncta along the long axis of the cell, rather than by diffusion of  
175 Pom1 molecules from the cell tips to the cell side.

176

### 177 ***In vitro* analysis shows Pom1 exists in large, stable puncta**

178 Past work suggested that Pom1 puncta assemble and disassemble at the cortex  
179 through oligomerization of individual molecules diffusing in the plane of the membrane  
180 (Saunders et al., 2012). However, our high-speed (20ms/frame) continuous TIRF videos  
181 suggested that Pom1 puncta bind and release the cortex as a pre-formed unit (Figure  
182 S2A). Consistent with this possibility, we observed rare cell lysis events in which Pom1  
183 puncta remained intact in extruded cytoplasm (Figure 2A). This apparent stability while  
184 removed from the plasma membrane led us to test the existence and properties of Pom1  
185 puncta in detergent cell extracts. Using TIRF microscopy, we observed puncta of Pom1-  
186 mNG in extracts made from Pom1-mNG cells, but not from untagged wild-type cells

187 **(Figure 2B)**. We next examined the size of these Pom1 puncta by velocity sucrose  
188 gradient sedimentation. By fractionating detergent cell extracts from *pom1-3xHA* cells,  
189 we found that most Pom1 exists in a large 60S complex, consistent with Pom1 puncta  
190 observed in cells. Fractions 6-8 containing this peak were dialyzed and centrifuged on a  
191 second sucrose gradient. These pooled fractions again sedimented at 60S, indicating that  
192 they represent a stable complex **(Figure 2C-D, S2B-C)**.

193  
194 Pom1 complexes present in detergent extracts resemble the cortical puncta  
195 observed in cells. To test this connection further, we examined the membrane-binding  
196 capacity of Pom1 complexes *in vitro* using artificial supported lipid bilayers (SLBs). Pom1-  
197 mNG puncta were isolated by sucrose gradient centrifugation, incubated with fluid SLBs  
198 on coverslips, and then imaged by TIRF microscopy **(Figure 2E, S2E)**. In this cell free-  
199 system, Pom1-mNG puncta bound and released SLB lipids with strikingly similar  
200 dynamics as in cells **(Figure 2E-F)**. Dwell times were increased for the kinase-dead  
201 mutant Pom1(K728R)-mNG, which was previously shown to increase cortical Pom1  
202 levels in cells **(Figure S2D)** (Bähler and Pringle, 1998; Hachet et al., 2011). Collectively,  
203 our TIRF microscopy and *in vitro* analysis of Pom1 puncta support a model whereby the  
204 majority of cellular Pom1 protein is contained within discreet, highly-stable oligomers that  
205 bind and release membranes with kinetics dictated by their catalytic activity in a geometric  
206 pattern that resembles a concentration gradient.

207  
208 Formation of clusters could represent an intrinsic property of Pom1 protein, or  
209 alternatively might require additional cellular factors. To distinguish between these  
210 possibilities, we expressed and purified GST-Pom1 from bacteria, and then performed  
211 sucrose gradient centrifugation experiments on this recombinant protein. Recombinant  
212 GST-Pom1 sedimented in a low molecular weight peak unlike Pom1 puncta from cells.  
213 Remarkably, purified GST-Pom1 was assembled into a puncta-sized high molecular  
214 weight complex by incubation with wild-type yeast detergent extract **(Figure 2G)**.  
215 Complex formation was also induced by incubation of GST-Pom1 with *pom1Δ* cell  
216 extracts, meaning that additional cellular factors drive this assembly process. **(Figure**  
217 **2G)**. Once assembled, Pom1 puncta are stable oligomeric complexes with intrinsic



218 membrane-binding properties that can be reconstituted *in vitro*. Additional cellular  
219 regulatory proteins are likely to promote the binding of Pom1 puncta at cell tips, leading  
220 to the spatial gradient.

## 221 222 **Polarity landmarks pattern cortical dynamics of Pom1 puncta to shape the gradient**

223 The key role of puncta in forming the Pom1 gradient led us to reexamine the role of  
224 cell polarity landmark proteins Tea1 and Tea4. Both of these proteins localize at cell tips  
225 and are required for proper Pom1 gradient formation ([Hachet et al., 2011](#)). However, past  
226 studies have shown that Tea1 and Tea4 have distinct mechanistic roles: Tea4 is required  
227 for localization of Pom1 to the cortex, whereas Tea1 is required for enrichment of cortical  
228 Pom1 to the cell tip ([Hachet et al., 2011](#)). We first used sucrose gradient centrifugation to  
229 test if either protein is required for assembly of Pom1 into stable biochemical complexes.  
230 The sedimentation pattern of Pom1 puncta isolated from *tea1* $\Delta$  and *tea4* $\Delta$  cells in velocity  
231 sucrose gradients is unchanged from wild-type cells, suggesting that neither Tea1 nor  
232 Tea4 are required for assembly of Pom1 into stable biochemical complexes (**Figure 3A**).  
233 Rather, these regulators are likely to act downstream of puncta assembly.

234  
235 We next tested the localization and dynamics of Pom1-mNG in *tea1* $\Delta$  and *tea4* $\Delta$  cells.  
236 Past work showed that membrane bound Tea4 is both necessary and sufficient to  
237 nucleate cortical Pom1 gradients, and this relationship is non-stoichiometric ([Hachet et](#)  
238 [al., 2011](#)). We confirmed that Pom1 was absent from the cell cortex in confocal  
239 micrographs of *tea4* $\Delta$  cells (**Figure 3B**). Surprisingly, we did observe Pom1-mNG puncta  
240 at the cortex of *tea4* $\Delta$  cells by TIRF microscopy (**Figure 3C**). These binding events  
241 occurred at lower frequency and had a shorter dwell time than in wild-type cells (**Figure**  
242 **3C-E**). Pom1-mNG puncta in *tea4* $\Delta$  cells were distributed evenly around the cell cortex  
243 with no detectable enrichment at tips. These infrequent, transient binding events do not  
244 result in accumulation of enough cortical Pom1 to be detected by confocal microscopy.  
245 Their rapid and position-independent association with the cortex leads to the absence of  
246 a cortical Pom1 gradient in *tea4* $\Delta$  cells.

247

248 In contrast, confocal micrographs of Pom1-mNG in *tea1* $\Delta$  cells confirmed even  
249 distribution around the entire cell cortex (**Figure 3B**). TIRF microscopy of *tea1* $\Delta$  cells  
250 revealed that this distribution arises from Pom1-mNG puncta, which bound the cell cortex  
251 at a frequency in between the tips versus sides of wild-type cells (**Figure 3C-D**). The  
252 duration of individual binding events was longer than in *tea4* $\Delta$  cells but shorter than in  
253 wild-type cells (**Figure 3E, S3A**). Thus, in *tea1* $\Delta$  cells Pom1 puncta bind at an  
254 intermediate frequency and for an intermediate duration, when compared to wild type and  
255 *tea4* $\Delta$  cells. These binding events are independent of spatial cues at the cell ends versus  
256 cell sides, resulting in enrichment of cortical Pom1 but not a gradient. Thus, Tea1 and  
257 Tea4 cooperate to promote localized membrane binding but not assembly of Pom1  
258 puncta. These spatial cues pattern the frequency of Pom1 puncta cortical interaction  
259 along the long axis of the cell.

260

#### 261 **Pom1 puncta interact with Cdr2 nodes at the lateral cortex**

262 It has been unclear when and where Pom1 interacts with its inhibitory target Cdr2,  
263 which localizes in cortical nodes positioned in the cell middle. Since Pom1 puncta appear  
264 to bind throughout the medial cell cortex, we used simultaneous two-color TIRF  
265 microscopy to test colocalization of Pom1 puncta and Cdr2 nodes. We observed  
266 unambiguous overlap between Cdr2 nodes and some Pom1 puncta, as well as Pom1  
267 puncta that bound to the cortex without encountering a Cdr2 node (**Figure 4A**). Thus,  
268 Pom1 puncta bind to the medial cortex in a stochastic pattern that can generate overlap  
269 with Cdr2 nodes. These patterns of colocalization were apparent in both static images  
270 and time-lapse movies (**Figure 4A-B**). The frequency, dwell time, and displacement of  
271 Pom1 cortical puncta were unaffected in *cdr2* $\Delta$  cells (**Figure S4A-DC**). These data  
272 suggest that Pom1 interacts with its inhibitory phosphorylation target Cdr2 when Pom1  
273 clusters associate with Cdr2 nodes at the medial cell cortex.

274

275 Phosphorylation by Pom1 prevents activation of Cdr2 in small cells, thereby  
276 contributing to cell size-dependent regulation of Wee1 and mitotic entry ([Allard et al., 2018](#)).  
277 To place this pathway in the context of Pom1 puncta and Cdr2 nodes, we analyzed  
278 how these structures accumulate and colocalize as cells grow. Intriguingly, the total

279 number of both Cdr2 nodes and Pom1 puncta detected in TIRF images all along cell sides  
280 were equivalent for cells of a given size (**Figure 4C-D**). The numbers of both structures  
281 show a similar size-dependent doubling. We next restricted our analysis to a  $2\mu\text{m} \times 2\mu\text{m}$   
282 square ROI positioned at the cell middle, where Cdr2 nodes concentrate. The local  
283 density of Cdr2 nodes in this region increased as a function of cell size, consistent with  
284 past studies ([Deng and Moseley, 2013](#); [Pan et al., 2014](#)). In contrast, the density of Pom1  
285 puncta in this region was largely independent of cell size (**Figure 4E**). In both TIRF and  
286 confocal images, the concentration of Pom1 protein and Pom1 clusters decreased slightly  
287 as cells increase in size, but this trend was dwarfed by the cell size-dependent increase  
288 in Cdr2 node density (**Figure 4E, S4D**). Thus, as cells grow larger, the ratio of Pom1 to  
289 Cdr2 in the medial cell cortex changes to favor Cdr2 because the densities of these two  
290 structures scale differently with cell size (**Figure 4G**).

291  
292 We next tested how this density scaling affects colocalization of Pom1 clusters and  
293 Cdr2 nodes as cells grow. Due to the increasing density of Cdr2 nodes, we observed an  
294 increased number of colocalized Pom1 clusters and Cdr2 nodes as cells increase in size  
295 (**Figure SE-F**). The increased colocalization, combined with the constant density of Pom1  
296 clusters, means that there are less “free” Pom1 clusters as cells increase in size (**Figure**  
297 **S4G**). Perhaps more importantly, the number of “free” Cdr2 nodes increased as a function  
298 of cell size (**Figure S4G**). These free Cdr2 nodes are not occupied by an inhibitory Pom1  
299 cluster, and thus have increased potential to promote mitotic entry by inhibiting Wee1. In  
300 this manner, Pom1 sets an inhibitory threshold that must be overcome by an increase in  
301 Cdr2 node density. The inhibitory threshold decreases slightly as cells grow, and  
302 functions most effectively in small cells, where Pom1 was previously shown to inhibit  
303 downstream signaling to Wee1 ([Allard et al., 2018](#)).

304  
305 **Control of Pom1 puncta levels in the medial cell cortex**

306 Our results suggest that Pom1 sets an inhibitory threshold that can be tuned by  
307 altering the concentration of Pom1 cortical clusters in the cell middle. We sought to test  
308 this model by increasing the abundance of Pom1 clusters in the cell middle. Low glucose  
309 media and *tea1* $\Delta$  are two independent conditions that disperse Pom1 throughout the

310 cortex, thereby increasing its concentration in the cell middle (Hachet et al., 2011; Kelkar  
311 and Martin, 2015) (See also **Figure S7A-C**). As a starting point, we tested the effect of  
312 mislocalized Pom1 in *tea1* $\Delta$  cells (**Figure 5A-B**). Surprisingly, higher Pom1 levels at the  
313 medial cortex did not impact the number of Cdr2 nodes or their recruitment of Wee1  
314 (**Figure 5C-F**). Past work showed that Pom1 retains kinase activity in *tea1* $\Delta$  cells (Bähler  
315 and Nurse, 2001), but several experiments suggested that this residual activity may be  
316 reduced. First, we compared *in vitro* kinase activity of Pom1 immunoprecipitated from  
317 *tea1* $\Delta$  cells or wild type cells. Pom1 from *tea1* $\Delta$  cells showed less kinase activity towards  
318 itself (autophosphorylation) and its substrate Cdr2 (**Figure S5A-C**). Second,  
319 phosphorylation of the Pom1 substrate Rga7 was reduced in *tea1* $\Delta$  cells (**Figure S5D-E**).  
320 Third, Tea4 is completely absent from the cortex of *tea1* $\Delta$  cells (**Figure S6D**). Catalytically  
321 active Pom1 autophosphorylates and requires Tea4-dependent dephosphorylation for  
322 cortical enrichment. Thus, in *tea1* $\Delta$  cells, Pom1 likely binds to the membrane because it  
323 cannot autophosphorylate properly. Finally, we note that Pom1 localization in *tea1* $\Delta$   
324 mimics the localization of kinase-dead *pom1-m2* mutant (**Figure S6A-B**). Therefore, we  
325 focused on the activity and regulation of Pom1 clusters in wild type cells grown in low  
326 glucose.

327  
328 Fission yeast cells respond to low glucose in part by depolymerizing their  
329 microtubule cytoskeleton, which leads to Pom1 redistribution to the lateral cell cortex  
330 where it delays mitotic entry (Kelkar and Martin, 2015). In time-lapse TIRF microscopy  
331 experiments, we observed increased numbers of discreet Pom1 puncta at the lateral cell  
332 cortex under low glucose conditions (**Figure 6A**). These puncta bound to the lateral cortex  
333 more frequently than under normal glucose conditions, but the average dwell time was  
334 unaffected (**Figure 6B-C**). This increased on-rate leads to accumulation of Pom1 clusters  
335 at the medial cell cortex.

336  
337 We next investigated how increased numbers of Pom1 puncta at the lateral cell  
338 cortex affect Cdr2 nodes using TIRF microscopy. In low glucose conditions, the number  
339 of Cdr2 nodes was largely unchanged, but the fluorescence intensity of individual Cdr2  
340 nodes and the overall concentration of Cdr2 at the medial cortex was significantly lower

341 **(Figure 6D-F, S7A-C)**. In *pom1* $\Delta$  cells, which grow only from one tip, Cdr2 nodes form  
342 normally but invade the non-growing tip. Low glucose conditions do not measurably affect  
343 Cdr2 nodes in *pom1* $\Delta$  cells, so the effects that we observed are Pom1-dependent **(Figure**  
344 **6D-F)**. These results indicate that Pom1 relocalization to the lateral cortex induces partial  
345 disassembly of Cdr2 nodes under low glucose. To quantify how this effect scales with  
346 glucose availability, we varied the concentration of media glucose over four orders of  
347 magnitude. Then, we measured the concentrations of both Pom1 and Cdr2 at both the  
348 cell sides and the cell tips. As glucose was reduced, Pom1 concentration decreased at  
349 cell tips and increased at cell sides, consistent with redistribution **(Figure 7A,C-D)**. In  
350 contrast, Cdr2 concentration increased at cell tips and decreased at cell sides **(Figure**  
351 **7B-D)**. Plots of glucose availability versus Pom1 or Cdr2 concentration produced  
352 sigmoidal curves with opposite orientations **(Figure 7C-D)**. Correlation analysis of Pom1  
353 and Cdr2 concentrations at cell sides show they are nearly perfectly anti-correlated  
354 (Pearson's  $r=-0.9352$ ,  $p=0.0006$ ) **(Figure 7E-F)**. We conclude that the increasing  
355 frequency of Pom1 cluster binding at the lateral cell cortex leads to progressive disruption  
356 of Cdr2 nodes.

357

### 358 **Pom1 disrupts Wee1 bursting under glucose deprivation**

359 We next examined the downstream effects of altered Pom1-Cdr2 signaling by  
360 using TIRF microscopy to monitor the previously described bursts of Wee1-mNG  
361 localization at Cdr2 nodes (Allard et al., 2018). In wild-type cells, both the frequency and  
362 duration of Wee1 bursts increased linearly with cell size, consistent with increased  
363 inhibition of Wee1 as cells grow **(Figure 8A,B)**. In low glucose, the frequency of Wee1-  
364 mNG bursts still scaled with cell size as in normal glucose. However, the duration of each  
365 burst was uniformly short and independent of cell size **(Figure 8A-B)**. These same burst  
366 properties were seen for Wee1-mNG bursts in kinase-dead *cdr2(E177A)* mutant cells  
367 grown in normal glucose **(Figure S8A-B)**. These results indicate that Cdr2 kinase activity  
368 is required for retention of Wee1 at nodes, but not for the initial binding event. Further,  
369 they demonstrate that low glucose phenocopies the kinase-dead mutant, consistent with  
370 Pom1-dependent inhibition of Cdr2 kinase activity.

371

372           These results suggested that attenuation of Wee1 bursting dynamics in low  
373 glucose might require Pom1 redistribution. We tested this idea by examining the glucose  
374 dependency of Wee1 node localization in *pom1* $\Delta$  cells. In *pom1* $\Delta$  cells growing under high  
375 glucose, the Wee1 burst frequency scales with cell size but Wee1 burst duration is  
376 uniformly high and independent of cell size (**Figure 8A,C**). Unlike wild type cells, which  
377 suppress Wee1 bursts in low glucose, *pom1* $\Delta$  cells show a striking increase in Wee1  
378 bursts under low glucose. This increase is not caused by burst duration, which was  
379 independent of both cell size and glucose concentration in *pom1* $\Delta$  cells. Rather, we  
380 measured increased Wee1-mNG burst frequency in low glucose *pom1* $\Delta$  cells (**Figure**  
381 **8A,C**). The reason for this increase is unknown, and suggests the existence of additional  
382 glucose-regulated pathways that operate on Cdr2-Wee1 signaling.

383  
384           Wee1 localization at Cdr2 nodes leads to its inhibitory phosphorylation by Cdr2  
385 and the related kinase Cdr1. To test how our TIRF-based localization results connect with  
386 Wee1 phosphorylation status, we analyzed phosphorylation-dependent shifts of Wee1  
387 migration using western blots (**Figure 8D**). In high glucose, Wee1 migrates as a smear  
388 of phosphorylated isoforms (Allard et al., 2018; Lucena et al., 2017). The upper,  
389 hyperphosphorylated forms are increased in *pom1* $\Delta$  cells but absent in *cdr2* $\Delta$  cells. This  
390 hyperphosphorylated Wee1 is lost in wild-type cells grown in low glucose, consistent with  
391 reduced bursts of Wee1 localization to nodes. In contrast, Wee1 appears even more  
392 hyperphosphorylated in *pom1* $\Delta$  cells grown under low glucose. This result suggests that  
393 Pom1 prevents phospho-inactivation of Wee1 in response to low glucose. These  
394 combined experiments support a model where Pom1 redistribution to the lateral cell  
395 cortex inactivates Cdr2 nodes to relieve inhibition of Wee1 under low glucose conditions.

396

## 397 **Discussion:**

398           In this study, we have shown that the Pom1 concentration gradient is generated  
399 by oligomeric Pom1 puncta that rapidly bind and release from the plasma membrane.  
400 These puncta bind more frequently at cell tips versus cell sides in high glucose media,  
401 while their binding rate is increased at cell sides in low glucose media. At the medial cell  
402 cortex, these puncta overlap with their inhibitory target Cdr2, which localizes in static

403 oligomeric nodes. More Cdr2 nodes are free from Pom1 inhibition as cells grow larger  
404 due to different density scaling of these two structures at the medial cell cortex. Our TIRF-  
405 based colocalization experiments on these structures were limited to short periods of time  
406 to avoid photobleaching, partly caused by the imaging conditions needed to observe  
407 these highly dynamic Pom1 clusters. Nevertheless, even over these short timescales of  
408 observation, the stochastic positioning of Pom1 puncta resulted in spatiotemporal  
409 colocalization with Cdr2 nodes. Given the high frequency of Pom1 puncta binding, we  
410 expect that many more colocalization events occur between Cdr2 nodes and Pom1  
411 clusters during the course of a full cell cycle, with the potential for Pom1 clusters to visit  
412 each Cdr2 node multiple times. Thus, these rapid dynamics of Pom1 puncta interacting  
413 with Cdr2 nodes must be integrated in time throughout the cell cycle, leading to the G2/M  
414 transition. It appears likely that the most critical temporal window for Pom1-Cdr2  
415 interactions occurs during early in G2, as *pom1* $\Delta$  show defects in Cdr2-Wee1 signaling  
416 specifically in small cells (Allard et al., 2018). It will be interesting to determine how these  
417 rapid interactions in small cells are integrated into the mitotic entry decision, which occurs  
418 later in the cell cycle when cells are longer.

419

## 420 **Molecular clusters are widespread in signal transduction**

421 The Pom1-Cdr2-Wee1 signaling pathway appears to function entirely within the  
422 confines of oligomeric protein clusters at the plasma membrane. The development of  
423 imaging technologies with increased spatial and temporal resolution has enabled the  
424 discovery of protein clustering as a paradigm in signaling. As a result, a growing number  
425 of signaling events and proteins have been found in similar clustered structures that are  
426 referred to as nanodomains, clusters, nanoclusters, and nodes, among other names. For  
427 example, recent studies have shown how PAR-3 polarity complexes in the *C. elegans*  
428 zygote form clusters to reduce random diffusion and promote vectorial transport  
429 (Dickinson et al., 2017; Munro, 2017; Rodriguez et al., 2017; Wang et al., 2017). In  
430 addition, major signal transduction pathways in plants are organized into protein clusters  
431 on plasma membrane nanodomains (Gronnier et al., 2017). Similarly, different Ras  
432 isoforms partition into distinct and exclusive clusters that digitize downstream signals in  
433 animal cells (Zhou and Hancock, 2015). In immune cells, both B-cell receptors and T-cell

434 receptors form oligomeric compartments at the cell cortex (Douglass and Vale, 2005; Liu  
435 et al., 2016; Maity et al., 2015). These T cell receptor clusters enrich downstream kinases  
436 while excluding phosphatases (Su et al., 2016), a mechanism that could relate to  
437 concentrated clusters of the kinases Pom1 and Cdr2. Clustering can have a range of  
438 critical impacts on the signaling properties of these pathways, such as the clustering of  
439 bacterial chemotactic receptors to generate signal amplification (Bray et al., 1998; Duke  
440 and Bray, 1999; Falke, 2002). Theoretical work has suggested that clustering can reduce  
441 noise by generating reaction bursts (Kalay et al., 2012), which have the capacity to  
442 overcome inhibitory thresholds, such as those imparted by phosphatases, more  
443 effectively than a system driven by gradual accumulation of signal. Insight into the  
444 functional role of clustering for Pom1-Cdr2-Wee1 will require additional *in vivo* analysis  
445 combined with *in vitro* reconstitution. We have shown that Pom1 clusters remain stable  
446 through biochemical enrichment, and isolated clusters exhibit the same membrane-  
447 binding properties *in vitro* as in cells. Past work has demonstrated Cdr2 nodes also remain  
448 stable through biochemical fractionation (Allard et al., 2018), providing the necessary  
449 tools for future dissection of the pathway in a reconstituted system.

450

### 451 **A new model for cortical gradient formation**

452 Our work has shown that Pom1 clusters bind to the cell cortex with different  
453 frequencies along the long axis of the cell, resulting in a concentration gradient. Past work  
454 suggested single Pom1 molecules (or small oligomers) bind to the membrane at tips, and  
455 then diffuse directionally away from the tip before dissociating (Hachet et al., 2011;  
456 Saunders et al., 2012). Clusters were proposed to dynamically assemble and  
457 disassemble at the cortex from this diffusing population (Saunders et al., 2012). Our  
458 findings suggest a new model for gradient formation, which is distinct from this previous  
459 model in four ways. First, we found that clusters themselves form a concentration gradient  
460 that emanates from the cell tips. Second, our combined imaging and biochemical  
461 approaches demonstrated that clusters are stable complexes that bind and rapidly  
462 release from the membrane. Third, we did not observe extensive diffusion by complexes  
463 bound to the membrane. It remains possible that smaller, diffusing Pom1 complexes or  
464 single molecules were not detected by our imaging approach, but we favor a model where



465 diffusion is limited to short, non-directional movements that do not contribute to gradient  
466 formation. Fourth, the key step in gradient formation is a positional system that increases  
467 the on-rate for Pom1 clusters at cell tips versus the cell middle. Concentration gradients  
468 are found across vast size scales in biology, so the mechanism of gradient formation by  
469 Pom1 clusters may have broad implications. It is also important to note that the spatial  
470 gradient of on-rates for Pom1 clusters binding to the cortex may depend on a  
471 concentration gradient of specific lipids in the plasma membrane. In support of this  
472 hypothesis, Pom1 binds to phosphatidylserine *in vitro* (Hachet et al., 2011), and this lipid  
473 is enriched at the tips of growing fission yeast cells (Haupt and Minc, 2017). Thus, further  
474 investigation of these lipids and their localization dynamics could reveal additional layers  
475 of this morphogen gradient.

476

477 We found that the polarity landmarks Tea1 and Tea4 provide the positional  
478 information for Pom1 clusters to form a concentration gradient. Past work has shown that  
479 Pom1 localizes homogenously throughout the cortex in *tea1* $\Delta$ , and does not localize to  
480 the cortex in *tea4* $\Delta$  (Bähler and Pringle, 1998; Hachet et al., 2011). Based on these and  
481 other results, Tea1 was proposed to recruit Tea4 to cell tips, where it promotes cortical  
482 loading of Pom1 molecules. Several results suggest that additional mechanisms may  
483 contribute to gradient formation. For example, we found that Pom1 clusters still bind to  
484 the cortex in *tea4* $\Delta$  cells but for very short durations. Past work has also shown that Tea1  
485 and Tea4 form cortical clusters that co-localize at cell tips, but these Tea1-Tea4 clusters  
486 do not co-localize with Pom1 clusters (Dodgson et al., 2013). Thus, Tea1-Tea4 may  
487 position binding of Pom1 clusters to the cortex through an additional mechanism. For  
488 example, Tea1 and Tea4 have been shown to assemble sterol-enriched lipid domains at  
489 cell tips when cells initiate polarization following exit from starvation (Makushok et al.,  
490 2016). Sterols and phosphatidylserine are thought to form a common membrane domain  
491 in fission yeast, suggesting that these proteins could act through the recruitment and  
492 organization of lipids to generate cortical domains permissive for Pom1 cluster binding  
493 (Haupt and Minc, 2017; Makushok et al., 2016).

494

495

## 496 **Adjustable Pom1 gradients regulate mitotic entry**

497 We propose an integrated mechanism for fission yeast cell size sensing in which  
498 Cdr2 acts as an important sensor of cell size that is dynamically antagonized by cortical  
499 Pom1 (**Figure 9**). Pom1 puncta bind to the medial cell cortex in a manner that can overlap  
500 with Cdr2 nodes. These dynamic Pom1 puncta and stable Cdr2 cortical nodes suggest a  
501 system that monitors surface expansion, consistent with the notion that fission yeast cells  
502 monitor surface area as the primary determinant of size at division ([Facchetti et al., 2019](#);  
503 [Pan et al., 2014](#)). As cells grow, the density of Pom1 clusters in the cell middle decreases  
504 slightly due to their binding preference at cell tips. In contrast, the density of Cdr2 nodes  
505 doubles to overcome this inhibitory Pom1 threshold. The density of Pom1 clusters and  
506 the resulting inhibitory threshold can be modulated by glucose availability, consistent with  
507 past work ([Kelkar and Martin, 2015](#)). As fission yeast cells begin to starve due to depletion  
508 of nutrients such as glucose, their length at division progressively decreases and the  
509 length of the cell cycle increases ([Pluskal et al., 2011](#); [Yanagida Mitsuhiro et al., 2011](#)).  
510 The Pom-Cdr2 network has a very prominent role in this nutrient modulation, suggesting  
511 that it may represent a key physiological role for the pathway ([Kelkar and Martin, 2015](#)).  
512 We found that the size dependence of Wee1 localization bursts to Cdr2 nodes, which  
513 facilitate Wee1 inhibition, was dampened in low glucose conditions. Re-localization of  
514 Pom1 clusters to the medial cortex likely mediates this response. However, for *pom1Δ*  
515 mutants in low glucose, Wee1 localization to nodes exceeds even wild type cells in high  
516 glucose. This result indicates that additional mechanisms contribute to Wee1 regulation  
517 in low glucose, for example Wee1 nuclear transport could be altered under these  
518 conditions.

519

## 520 **The Pom1 gradient as a read-out for cell polarity**

521 More broadly, our study reveals the adjustable nature of the concentration gradient  
522 formed by Pom1 clusters. Concentration of Pom1 clusters at cell tips reads out the polarity  
523 state of the cell for downstream signaling by Cdr2 and Wee1. Conditions that alter the  
524 polarized growth state of the cell would lead to changes in the gradient of Pom1 clusters,  
525 resulting in altered cell size at division. This dynamic system appears to operate in a  
526 manner that depends on both cell size and nutrient availability. Identification of additional

527 growth and environmental conditions that alter the relative distributions of Pom1 clusters  
528 and Cdr2 nodes, and determination of how they connect with other cell cycle signaling  
529 pathways, may reveal new mechanisms for nutrient modulation of cell size control.

530

### 531 **Integration of the Pom1-Cdr2-Wee1 pathway with other sizing mechanisms**

532 Pom1-Cdr2-Wee1 signaling is cell size dependent but is not the only pathway that  
533 contributes to the overall cell size control network. Intriguingly, a recent study reported  
534 that *cdr2Δ* cells no longer divide based on accumulation of a threshold surface area and  
535 instead revert to a secondary mechanism of cell size control based on volume sensing.  
536 These results demonstrate that cells use different signal transduction networks to  
537 measure different aspects of their size. Whereas the Pom1-Cdr2 network is well suited to  
538 measure cortical surface area, size-control systems that measure other aspects of size  
539 would require different signaling logic. Theoretically, mechanisms for cell volume sensing  
540 could depend on proteins whose concentrations do not scale linearly with cell size. Such  
541 mechanisms are thought to underlie cell size control in other organisms, such as the  
542 budding yeast, where growth-dependent dilution of the transcriptional repressor Whi5 is  
543 thought to underlie G<sub>1</sub>/S size control ([Schmoller et al., 2015](#)). One possible candidate for  
544 cellular volume sensing in fission yeast is Cdc25, which increases in concentration with  
545 cell size ([Keifenheim et al., 2017](#); [Moreno et al., 1990](#)). These mechanisms are attractive  
546 candidates for volume sensors because cytoplasmic concentration is independent of cell  
547 geometry. The existence of sizing mechanisms that measure other aspects of cell size,  
548 and function independently of the Pom1-Cdr2 surface area sensing network, underscores  
549 that cell size is a systems level property controlled by multiple signaling pathways. Thus,  
550 it remains important to discover size-dependent signaling mechanisms within each  
551 individual pathway, as a step towards understanding the integration of multiple pathways  
552 into a larger size control system.

553

554

555

556

557

## 558 **Materials and Methods:**

### 559 **Strain Construction and Media**

560 Standard *S. pombe* media and methods were used (Moreno et al., 1991). Strains  
561 used in this study are listed in Supplementary Table S1. Gene tagging and deletion were  
562 performed using PCR and homologous recombination (Bähler et al., 1998). The  
563 mNeonGreen (mNG) sequence was used under license from Allele Biotechnology.

564

### 565 **TIRF Microscopy and Analysis**

566 Pom1 puncta and node components were imaged using simultaneous dual-color  
567 total internal reflection fluorescence microscopy to limit excitation of fluorophores to those  
568 nearest to coverslip. Imaging was performed on a commercially available TIRF  
569 microscope (Micro Video Instruments) composed of a Nikon Eclipse Ti microscope base  
570 equipped with a 100x Nikon Apo TIRF NA 1.49 objective and a two-camera imaging  
571 adaptor (Tu-CAM, Andor Technology) containing a dichroic and polarization filters  
572 (Semrock FF580-FDi01-25x36, FF02-525/40-25, FF01-640/40-25) to split red and green  
573 signal between two aligned Andor iXon electron-multiplied CCD cameras (Andor  
574 Technology). Red/green beam alignment was performed prior to imaging using a  
575 TetraSpeck Fluorescent Microsphere size kit (Thermofisher).

576

577 Standard #1.5 glass coverslips were RCA cleaned before use to remove  
578 fluorescent debris. Cells were grown in EMM4S, and washed into fresh EMM4S  
579 immediately before imaging to remove auto-fluorescent debris resulting from overnight  
580 culture. Cells were imaged in EMM4S media on glass slides at ambient temperature.  
581 Individual slides were used for no more than five minutes to prevent cells from exhausting  
582 nutrients or oxygen. Agar pads were not used due to increased background fluorescence.

583

584 Image analysis and processing was performed using ImageJ2 (NIH). Cdr2 node  
585 numbers and Pom1/Wee1 puncta number, frequency and binding duration were  
586 quantified using the Trackmate plugin (Tinevez et al., 2017). Due to variable fluorescence  
587 intensity in different TIRF fields and images, thresholding parameters were determined  
588 separately for each image, and accuracy was confirmed by visual inspection to ensure

589 that only nodes/puncta were counted and that no nodes/puncta were omitted. For Wee1  
590 burst and Pom1 puncta tracking, Particle Diameter was set to 0.3 microns (approximate  
591 lateral resolution), with Maximum Gap Linking set to 2 frames, and Linking Range for  
592 particle tracking was set to 0.15 microns. Lookup table was adjusted to fire for some  
593 images to emphasize signal intensities.

594

### 595 **“Head-On” Tip Imaging**

596 “Head-On” or “Tip” imaging was performed using a protocol modified from  
597 (Dodgson et al., 2013). Custom micro-well coverslips or Ibidi Sticky-Slide VI channels  
598 (Ibidi, Martinsried, Germany) were coated with BS-I lectin (1mg/mL in water) by incubation  
599 for 30 minutes and washed 3X with water to remove non-adherent lectin. Cells were then  
600 added to the imaging chambers and allowed to settle to the cover-slip bottom where they  
601 adhere to the lectin. Cells oriented with the long axis perpendicular to the coverslip were  
602 identified using brightfield prior to fluorescence imaging.

603

### 604 **Spinning Disc Microscopy and Analysis**

605 Spinning-disc confocal imaging was performed using a commercially available  
606 system (Micro Video Instruments, Avon, MA) featuring a Nikon Eclipse Ti base equipped  
607 with an Andor CSU-W1 two-camera spinning disc module, dual Zyla sCMOS cameras  
608 (Andor, South Windsor, CT) an Andor ILE laser module, and a Nikon 100X Plan Apo  $\lambda$   
609 1.45 oil immersion objective. Cells were imaged in EMM4S media on glass slides at  
610 ambient temperature unless otherwise noted.

611

### 612 **Airyscan Super-Resolution Microscopy and Analysis**

613 To achieve maximum resolution and sensitivity, fluorescence intensity of Pom1  
614 puncta on both cell sides and cell tips was measured using a Zeiss Airyscan microscope  
615 (**Figure S1I-K**), composed of a Zeiss LSM-880 laser scanning confocal microscope  
616 (Zeiss, Oberkochen, Germany) equipped with 100X alpha Plan-Apochromat/NA 1.46 Oil  
617 DIC M27 Elyra objective, Airyscan super-resolution module and GaAsP Detectors, and  
618 Zen Blue acquisition software using the Super-resolution mode with pin-hole size of 1.2  
619 airy-units to prioritize resolution. Z-volumes of 16 slices with 0.19 $\mu$ m spacing for high

620 spatial resolution in all dimensions were centered on the cell cortex closest to the  
621 coverslip. Airyscan images were processed in Zeiss Zen Blue software, and quantification  
622 was performed on sum projections of Airyscan reconstructed stacks.

623

### 624 **Pom1 and Cdr2-CTD Purification**

625 The full length Pom1 sequence, and the Cdr2-CTD fragment were purified as  
626 follows: Each sequence was subcloned into pGEX6P1 vector using the Xho1 restriction  
627 site and expressed as a GST-fusion protein in *Escherichia coli* strain BL21(DE3).  
628 Transformants were cultured to log-phase at 37°C, followed by a shift to 25°C for 30  
629 minutes. Expression was then induced by addition of 1-thio-β-D-galactopyranoside to  
630 200μM, followed by growth for an additional 3 hours at 25°C. Cells were harvested by  
631 centrifugation and lysed by passing them twice through a French press in lysis buffer  
632 (1xPBS, 100mM NaCl, 1mM DTT, and complete EDTA-free protease inhibitor tablets (1  
633 tablet/50mL Buffer) (Roche, Basel, Switzerland)). Following lysis, Triton-X 100 was added  
634 to 1% V/V. Lysates were then cleared by centrifugation for 10 minutes at 12,000 x g at  
635 4°C in a Sorval SS-34 fixed-angle rotor (Thermo Scientific, Waltham, MA). The  
636 supernatant was then incubated with glutathione-agarose (Sigma Aldrich, St. Louis, MO)  
637 for 2h at 4°C. 20 mM glutathione (pH 8.0) was used to elute purified protein, and the  
638 eluate was dialyzed overnight at 4°C into 10mM Tris-HCl, pH8 + 5% V/V glycerol.

639

### 640 **Preparation of Yeast Extracts**

641 Fission yeast detergent extracts were prepared by growing 1.5L cells to mid-log  
642 phase (OD ~0.3), and then washed twice with 50mL Node Isolation Buffer (NIB – 50mM  
643 HEPES, 100mM KCl, 1mM MgCl<sub>2</sub>, 1mM EDTA, pH 7.5) (Allard et al., 2018). Next, we  
644 resuspended the pellet in an equal volume of 2X NIB (W/V) containing a  
645 protease/phosphatase inhibitor cocktail (10μL/mL 200x PI, 50μL/mL 1M β-glycerol  
646 phosphate, 50μL/mL 1M NaF, 2.5 μL/mL 200mM PMSF, 1mM DTT), and snap froze the  
647 resuspension as pellets by pipetting drop-wise into a liquid nitrogen bath. Then, yeast  
648 pellets were ground using liquid-nitrogen chilled coffee-grinders for 2 min, and collected  
649 into chilled falcon tubes and stored at -80°C. 1.5g of frozen yeast powder was then thawed  
650 on ice, and Triton X-100 was added to a final concentration of 1%, and the extracts were

651 mixed by gentle pipetting. Extracts were then centrifuged at 4°C for 10min at 20,000 x g  
652 to yield a low speed supernatant, which were then used for subsequent experiments.

653

### 654 **Sucrose Gradient Ultracentrifugation**

655 Discontinuous sucrose gradients were prepared in 14 x 89mm Ultra Clear  
656 Ultracentrifuge tubes (Beckman Coulter, Brea, CA) by layering 5 – 23% (top to bottom)  
657 sucrose in NIB + 1% Triton X-100 in 0.37mL steps of 2% sucrose increments. 700µL of  
658 yeast extract or recombinant protein diluted in NIB Buffer was then added to the top of  
659 the gradient. Sucrose gradients were centrifuged at 100k x g (50kRPM) in a Beckman L8-  
660 M ultracentrifuge for 2hr at 4°C in a chilled SW60ti swinging bucket rotor. 0.5mL gradient  
661 fractions were collected from the top by hand, vortexed, and 100µL of each fraction was  
662 mixed 2:1 in 3X SDS-PAGE sample buffer (65 mM Tris pH 6.8, 3% SDS, 10% glycerol,  
663 10% 2-mercaptoethanol, 50 mM NaF, 50 mM β-glycerophosphate, 1 mM sodium  
664 orthovanadate) and boiled for 5 min. Samples were then subjected to SDS-PAGE and  
665 western blotting or Coomassie staining. To calculate S-values of sedimentation peaks  
666 from western blot signal intensities, mean band intensities were measured using Image  
667 Studio Lite (LICOR, Lincoln, NE), and Gaussian Curves were fit to these values. The peak  
668 of the Gaussian for each sedimentation peak of each protein was used to assign the  
669 known or interpolated S-value.

670

### 671 **Western Blotting**

672 For western blots, cells were lysed in 150 µl of 3X SDS-PAGE sample buffer with  
673 glass beads in a Mini-beadbeater-16 (Biospec, Bartlesville, OK) for 2 minutes. Gels were  
674 run at a constant 20 mAmps until 75kDa marker was at the bottom of the gel. Blots were  
675 probed with anti-HA (Covance, Princeton, NJ) or homemade anti-GST. For monitoring  
676 Wee1 phosphorylation, samples were run on an SDS-PAGE gel containing 6%  
677 acrylamide and 0.02% bisacrylamide, and then probed with a homemade anti-Wee1  
678 antibody (Allard et al., 2018).

679

### 680 **Supported Lipid Bilayers**

681 To prepare supported lipid bilayers, we first prepared small unilamellar vesicles  
682 (SUVs) composed of three lipids: (1) DOPC (18:1 (Delta9) Cis PC - 1,2 Dioleoyl-sn-  
683 glycerol-3-phosphocholine), (2) DOPS (18:1 PS - 1,2-Dioleoyl-sn-Glycerol-3-[Phospho-L-  
684 Serine]), and (3) fluorescent 18:1 Liss Rhod PE (1,2-dioleoyl-sn-glycerol-3-  
685 phosphoethanolamine-N-(lissamine rhodamine B sulfonyl). All lipids were dissolved in  
686 chloroform (Avanti, Alabaster, AL). 2µmol total lipid with the desired molar ratios were  
687 mixed in glass vials with PTFE coated caps, which had been RCA cleaned and rinsed  
688 three times with chloroform before use. Excess chloroform was evaporated in a vacuum  
689 desiccator for 1 hour. Lipids were resuspended in 400µL SUV Buffer (50mM HEPES,  
690 100mM KCl, 1mM EDTA, 1mM MgCl<sub>2</sub>, pH7.5) for 5mM lipid mixture stocks. The lipid  
691 mixtures were vortexed until cloudy, and then transferred to 1.5mL Eppendorf tubes and  
692 subjected to ten freeze-thaw cycles using a liquid nitrogen bath and 32°C hot plate, with  
693 2 minutes of sonication in a sonicating water bath following each thaw cycle. Stocks were  
694 stored at -80°C in 20µL aliquots.

695  
696 Supported lipid bilayers were made by adding 10µL of SUVs to RCA cleaned  
697 custom microwells built on 22x40mm #1.5 coverslips. Chambers were then incubated at  
698 37°C for one hour to induce vesicle fusion, and unincorporated vesicles were rinsed away  
699 using five rinses with 100µL SUV buffer. Yeast extract was added to these chambers by  
700 removing 90µL of buffer, leaving just enough to cover the chamber bottom, and then  
701 adding extract.

702  
703 **Pom1 Immunoprecipitation**

704 Cultures were grown in EMM4S media to log phase, and a volume equivalent to  
705 200 optical density units were harvested by centrifugation. The pellet was washed in  
706 Wash Buffer (1X PBS, 250mM NaCl, 1mM EDTA, 1mM PMSF, 50mM NaF, 50mM β-  
707 glycerophosphate, 1mM sodium orthovanadate, and 1% Triton X-100, and complete  
708 EDTA-free protease inhibitor cocktail (1 tablet/50mL) (Roche)). The pellet was then  
709 resuspended in 5mL of wash buffer, and divided into 1.5mL screw-cap tubes each with  
710 200µL glass beads for lysis by bead-beating for 2 minutes using a mini-Beadbeater-16  
711 (Biospec) at 4°C. Lysates were cleared by centrifugation at 16,000 x g for 10 minutes at



712 4°C in an Eppendorf 5415C centrifuge. The supernatant was then incubated with rotation  
713 at 4°C for 1 hour with Pierce anti-HA magnetic beads (Thermo Scientific). Beads were  
714 washed five times for 15 minutes each in Wash Buffer prior to use. Beads were  
715 resuspended in Kinase Assay Buffer (see below) for immediate use in kinase assays.

716

### 717 ***In vitro* kinase assays**

718 For *in vitro* kinase assays, immunoprecipitated Pom1 proteins and purified Cdr2-  
719 CTD were combined at a 1:1 ratio in Kinase Assay Buffer (20mM Tris pH 8, 100mM NaCl,  
720 50mM NaF, 50mM  $\beta$ -glycerophosphate, 1mM sodium orthovanadate, 10mM MgCl<sub>2</sub>,  
721 20 $\mu$ M ATP- $\gamma$ -S) for 30 minutes at 30°C. The reaction was halted by addition of EDTA to  
722 20mM. For subsequent analysis by anti-thiophosphate western blot, proteins in *in vitro*  
723 kinase assays were then alkylated by addition of p-nitrobenzyl mesylate to 2.5mM, and  
724 incubation at 25°C for one hour. Samples were then prepared for western blot as  
725 described above. Thiophosphate western blots were probed with an antibody against  
726 thiophosphate-ester (Abcam 92570) (Abcam, Cambridge, United Kingdom).

727

728

729

## 730 **Figure Legends:**

731

732 **Figure 1: The Pom1 gradient is formed by time-averaging of puncta that transiently**  
733 **bind the cortex with different dynamics along the long axis of the cell. (A)** Individual  
734 frame (top panel) and sum projections (bottom panel) of high-speed TIRF microscopy  
735 movie. Scale bar 1 $\mu$ m. Movie was continuous 15s time-lapse acquisition of 200ms  
736 exposures. Blue arrows mark position of line scans performed for data in panel B. **(B)**  
737 Line scans of fluorescence intensity along the long axis of the snap shot and projection  
738 images in panel (A). Note that time-averaging of Pom1 puncta smoothens the  
739 concentration gradient. **(C)** Traces of single-particle diffusion paths generated from a 15s  
740 time-lapse TIRF microscopy acquisition of Pom1-mNeonGreen. Scale bar 1 $\mu$ m. **(D-E)**  
741 Pom1-mNeonGreen forms puncta both at the cell tip and cell side. Images are sum  
742 projections of three consecutive 200ms exposures from continuous time-lapse TIRF

743 microscopy acquisitions of either the cell tip or side as depicted in the cartoon diagrams.  
744 Scale bar 1 $\mu$ m. **(F-H)** Particle-tracking analysis of 2 $\mu$ m x 2 $\mu$ m ROIs from 30s continuous  
745 time-lapse TIRF acquisitions of Pom1-mNeonGreen at either the cell tip or side was used  
746 to measure and compare (F) the binding frequency of Pom1 puncta (\*\*\*\*,  $p<0.0001$ ),  
747 (G) the average displacement of individual puncta (\*\*\*,  $p=0.0002$ ), (H) the binding  
748 duration of individual puncta (n.s.,  $p=0.6747$ ). Each data point represents a single cell  
749 mean, and line and error bars represent mean and standard deviation of all cells.  
750 Statistical significance was tested using a Student's T-test. **(I)** Histogram of the  
751 fluorescence intensity of individual Pom1 puncta at the cell tip and cell side. Puncta were  
752 binned by fluorescence intensity and displayed as a population frequency.

753  
754 **Figure 2: Pom1 puncta are stable structures that can be isolated *in vitro*.** **(A)** TIRF  
755 microscopy image reveals fluorescent puncta in the extruded cytoplasm (white dotted  
756 line) from a lysed Pom1-mNeonGreen cell (yellow dotted line). Scale bar 5 $\mu$ m. **(B)** TIRF  
757 microscopy images of cell extracts prepared from wild-type (no tag) or Pom1-  
758 mNeonGreen cells. Images are 50 frame sum projections of continuous 200ms time-lapse  
759 exposures. The two images were contrasted equally. Scale bar 1 $\mu$ m. **(C)** Cytoplasmic  
760 extracts of *pom1-3HA* cells were subjected to velocity sucrose gradient sedimentation,  
761 and fractions were probed against the HA tag (upper blot). Fraction 1 corresponds to the  
762 top of the gradient and contains smaller structures; fraction 12 corresponds to bottom of  
763 the gradient and contains larger structures. Fractions 6-8 were pooled, sucrose was  
764 removed by dialysis, and then the sample was subjected to a second identical round of  
765 sucrose gradient sedimentation and western blotting of the resulting fractions (lower blot).  
766 **(D)** Quantification of Pom1-3HA band intensities from western blot of yeast extracts in  
767 panel C. Each apparent peak was fit to a gaussian curve, and S-values were determined  
768 using size-standards run on identical gradients. **(E)** TIRF microscopy of Pom1-mNG  
769 puncta from cytoplasmic extracts on supported lipid bilayers. Scale bar 1 $\mu$ m. Left panel  
770 is single time point image. Right panel is kymograph taken from line scan of time-lapse  
771 TIRF experiment. **(F)** Quantification of binding duration of Pom1-mNG puncta on  
772 supported lipid bilayers by TIRF microscopy as in panel F. Values are compared to  
773 cellular measurements of pooled tip and side localized Pom1 puncta (n.s.,  $p=0.0514$ ). **(G)**

774 Purified GST-Pom1 was subjected to sucrose gradient sedimentation and the fractions  
775 were probed against the GST tag (upper blot). Purified GST-Pom1 was also added into  
776 wild-type cell or *pom1* $\Delta$  cell extracts and incubated for 1hr at 4°C in the presence of ATP  
777 before velocity sucrose sedimentation and western blotting (bottom blots).

778  
779 **Figure 3: Polarity landmarks pattern cortical dynamics of Pom1 puncta to shape the**  
780 **gradient. (A)** Western blots of sucrose gradient fractions after sedimentation analysis as  
781 in Figure 1C of extracts prepared from *tea1* $\Delta$  or *tea4* $\Delta$  cells expressing Pom1-3HA. **(B)**  
782 Confocal micrographs of Pom1-mNG in *tea1* $\Delta$  or *tea4* $\Delta$  cells. Images are from the middle  
783 focal plane; scale bar 5 $\mu$ m. **(C)** TIRF micrographs of Pom1-mNG localization at the tip or  
784 side cortex in *tea1* $\Delta$  or *tea4* $\Delta$  cells. Scale bar 1 $\mu$ m. **(D)** The mean binding frequency of  
785 Pom1-mNG puncta at the tips and sides of wild-type, *tea1* $\Delta$  or *tea4* $\Delta$  cells, measured by  
786 TIRF microscopy. **(E)** The mean binding duration of Pom1-mNG puncta at the tips and  
787 sides of wild-type, *tea1* $\Delta$  or *tea4* $\Delta$  cells, measured by TIRF microscopy. For D-E, wild-  
788 type data are replotted from Figure 1. Each data point represents a single cell mean, and  
789 line and error bars represent mean and standard deviation of all cells. Comparisons are  
790 1-way ANOVA with Tukey's multiple comparisons tests. \*\*\*\* indicates  $p < 0.0001$ , n.s.  
791 indicates  $p > 0.05$ .

792  
793 **Figure 4: Scaling of Pom1 puncta and Cdr2 nodes at the lateral cell cortex. (A)** A  
794 subset of Pom1 puncta colocalize with Cdr2 nodes. Images are dual-channel  
795 simultaneously-acquired TIRF microscopy images of cells expressing Pom1-mNG and  
796 Cdr2-tagRFP-t. Yellow dashed brackets outline the ROI of the lower zoomed panels.  
797 Orange arrows point to Pom1 puncta colocalized with Cdr2 nodes. Scale bar is 1 $\mu$ m. **(B)**  
798 Kymographs generated using the ROI drawn on the merged zoom image in panel A. Cyan  
799 arrows indicate prominent Pom1 puncta, magenta arrows indicate prominent Cdr2 nodes,  
800 and orange arrows adjacent to the merged kymograph indicate colocalization. **(C)**  
801 Localization of Cdr2-mEGFP (upper panels) or Pom1-mNG (lower panels) in  
802 representative cells of increasing size by TIRF microscopy. Scale bar is 1 $\mu$ m. **(D)** Total  
803 number of Cdr2-mEGFP nodes (blue circles) or Pom1-mNG puncta (red squares)  
804 measured per cell by TIRF microscopy. Quantification is limited to puncta detected and

805 resolvable in the TIRF illumination field. The slopes of the corresponding linear  
806 regressions are not significantly different ( $p=0.3757$ ). **(E)** Density of Cdr2-mEGFP nodes  
807 (blue circles) or Pom1-mNG puncta (red squares) in  $2 \times 2 \mu\text{m}$  square ROIs at the cell middle  
808 using TIRF microscopy. **(F)** Example of colocalization analysis for Pom1 puncta and Cdr2  
809 nodes. The spot detection algorithm in TrackMate plugin for ImageJ2 was used to assign  
810  $0.3 \mu\text{m}$  diameter circular ROIs to Cdr2 nodes (cyan) and Pom1 puncta (magenta) in  
811 images such as panel A. Structures were counted as colocalized if the ROI assigned to  
812 one channel overlapped with the middle of the ROI of the other channel (right panel,  
813 yellow circles). Adjacent structures that failed this criterion were deemed not to be  
814 colocalized (right panel, grey circles). **(G)** Ratio of free Cdr2 nodes to free Pom1 puncta,  
815 plotted as a function of cell size.

816

817 **Figure 5: Properties of Pom1 puncta in *tea1* $\Delta$  cells.** **(A)** Localization of Pom1-mNG in  
818 wild-type or *tea1* $\Delta$  cells imaged by confocal microscopy at focal planes in the cell middle.  
819 Scale bar,  $5 \mu\text{m}$ . **(B)** Comparison of Pom1 concentration along  $2 \mu\text{m}$  cortical line scans  
820 positioned at the cell middle of wild-type and *tea1* $\Delta$  cells, from images as in panel A.  
821 Significance was tested using a Student's T-test (\*\*\*\*,  $p < 0.0001$ ). **(C)** Localization of  
822 Cdr2-mNG in *tea1* $\Delta$  cells by TIRF microscopy. Scale bar is  $5 \mu\text{m}$ . **(D)** Number of Cdr2-  
823 mNG nodes as a function of cell length in wild-type (blue circles) or *tea1* $\Delta$  cells (red  
824 squares), measured using TIRF microscopy images as in panel C and Figure 5A. The  
825 slopes of the linear regression of each data set do not differ significantly from each other  
826 ( $p=0.2029$ ). **(E)** Localization of Wee1-mNG in *tea1* $\Delta$  cells by TIRF microscopy. Scale bar  
827 is  $5 \mu\text{m}$ . **(F)** Number of Wee1-mNG bursts as a function of cell length in wild-type (blue  
828 circles) or *tea1* $\Delta$  cells (red squares), measured using TIRF microscopy images as in panel  
829 E and Figure 7A. There is a small but significant difference in the slopes of the linear  
830 regressions ( $p=0.0158$ ) such that the number of Wee1-mNG bursts scales more slowly  
831 in *tea1* $\Delta$  cells than in WT. This discrepancy may result because *tea1* $\Delta$  cells can be bent  
832 or T-shaped, rendering length an imperfect proxy for size.

833

834 **Figure 6: Redistribution of Pom1 puncta to the lateral cortex disrupts Cdr2 nodes**  
835 **during glucose restriction.** **(A)** Localization of Pom1-mNG in wild-type cells grown in

836 either high (2%) or low (0.03%) glucose media. Images were collected using TIRF  
837 microscopy. Scale bar, 5 $\mu$ m. **(B)** Comparison of the binding frequency of Pom1 puncta at  
838 the lateral cell cortex in cells grown under high and low glucose measured using TIRF  
839 microscopy (\*\*\*,  $p=0.0003$ ). Statistical significance was tested using a Student's T-test.  
840 **(C)** Comparison of the binding duration of Pom1 puncta at the lateral cell cortex in cells  
841 grown under high and low glucose measured using TIRF microscopy (n.s.,  $p=0.6833$ ).  
842 Statistical significance was tested using a Student's T-test. **(D)** Localization of Cdr2-mNG  
843 in wild-type or *pom1* $\Delta$  cells grown in either normal (2%) or low (0.03%) glucose media.  
844 Images were collected using TIRF microscopy. Scale bar, 1 $\mu$ m. **(E)** Comparison of the  
845 fluorescence intensity of individual Cdr2-mNG nodes in wild-type or *pom1* $\Delta$  cells grown  
846 in either normal (2%) or low (0.03%) glucose media. Cdr2 nodes in wild-type cells become  
847 significantly smaller under low glucose conditions (\*\*\*\*,  $p<0.0001$ ), but there is no  
848 significant difference in Cdr2 nodes size in *pom1* $\Delta$  cells grown in normal vs low glucose  
849 (n.s.,  $p=0.4015$ ). Measurements were taken from Airyscan Super-Resolution confocal  
850 micrographs. **(F)** Quantification and comparison of the total number of Cdr2-mNG nodes  
851 visible in TIRF micrographs of wild-type or *pom1* $\Delta$  cells grown in either normal (2%) or  
852 low (0.03%) glucose media. There is no significant difference in any condition ( $p>0.05$ ).  
853 Statistical significance was tested using a one-way ANOVA.

854  
855

856 **Figure 7: Pom1 and Cdr2 concentrations at the lateral cell cortex are anti-correlated.**

857 **(A)** Localization of Pom1-mNG in confocal micrographs at middle cell focal planes.  
858 Regions where line-scans were used to measure fluorescence intensity are marked at  
859 the tip and side (orange lines). Scale bar, 1 $\mu$ m. **(B)** Localization of Cdr2-mNG in confocal  
860 micrographs at middle cell focal planes. Scale bar, 1 $\mu$ m. Regions where line-scans were  
861 used to measure fluorescence intensity are marked at the tip and side (orange lines). **(C)**  
862 Concentration of Pom1 (red squares) or Cdr2 (blue circles) at cell sides in a range of  
863 glucose concentrations, measured using 'Side ROI' denoted in panels A and B. **(D)**  
864 Concentration of Pom1 (red squares) or Cdr2 (blue circles) at cell tips in a range of  
865 glucose concentrations, measured using 'Tip ROI' denoted in panels A and B. **(E)**  
866 Correlation of Cdr2 vs Pom1 concentrations at cell sides in each glucose concentration

867 from panel C. Concentrations are anticorrelated across all tested media glucose  
868 concentrations ( $p=0.0006$ , Pearson  $r=-0.9352$ ). **(F)** Correlation of Cdr2 vs Pom1  
869 concentrations at cell tips in each glucose concentration from panel D. Concentrations  
870 show weak anticorrelation across the tested media glucose concentrations, but the  
871 correlation is not statistically significant ( $p=0.09$ , Pearson  $r=-0.65$ ).

872

873 **Figure 8: Pom1 redistribution under glucose restriction disrupts Wee1 regulation at**  
874 **cortical nodes. (A)** Localization of Wee1-mNG in wild-type or *pom1* $\Delta$  cells grown in  
875 either high (2%) or low (0.03%) glucose media. Images were collected using TIRF  
876 microscopy. Scale bar, 5 $\mu$ m. **(B)** Quantification of Wee1 bursting kinetics in wild-type cells  
877 grown under high (2%, blue circles) and low (0.03%, red squares) glucose conditions.  
878 The top panel is a plot of the total number of Wee1 bursts as a function of cell length,  
879 counted in single time point TIRF micrographs. The slopes of the linear regressions are  
880 significantly different ( $p<0.0001$ ,  $R^2_{2\%}=0.66$ ,  $R^2_{0.03\%}=0.45$ ). The middle panel is a plot of  
881 the frequency of Wee1 bursts as a function of cell length, measured using the TrackMate  
882 particle tracking algorithm on TIRF microscopy movies. The slopes of the linear  
883 regressions are not significantly different ( $p=0.8426$ ,  $R^2_{2\%}=0.50$ ,  $R^2_{0.03\%}=0.51$ ). The  
884 bottom panel is a plot of Wee1 burst duration as a function of cell length, measured using  
885 the TrackMate particle tracking algorithm on TIRF microscopy movies. The slopes of the  
886 linear regressions are not significantly different ( $p=0.09$ ,  $R^2_{2\%}=0.28$ ,  $R^2_{0.03\%}=0.05$ ), but the  
887 values of the elevation of the regressions are significantly different ( $p=0.0005$ ). **(C)**  
888 Quantification of Wee1 bursting kinetics in *pom1* $\Delta$  cells grown under normal (2%, green  
889 circles) and low (0.03%, magenta squares) glucose conditions. The top panel is a plot of  
890 the total number of Wee1 bursts as a function of cell length, counted in single time point  
891 TIRF micrographs. The slopes of the linear regressions are not significantly different  
892 ( $p=0.09$ ,  $R^2_{2\%}=0.45$ ,  $R^2_{0.03\%}=0.54$ ), but the values of the elevation of the regressions are  
893 significantly different ( $p<0.0001$ ). The middle panel is a plot of the frequency of Wee1  
894 bursts as a function of cell length, measured using the TrackMate particle tracking  
895 algorithm on TIRF microscopy movies. The slopes of the linear regressions are not  
896 significantly different ( $p=0.3125$ ,  $R^2_{2\%}=0.45$ ,  $R^2_{0.03\%}=0.56$ ) but the values of the elevation  
897 of the regressions are significantly different ( $p=0.009$ ). The bottom panel is a plot of Wee1

898 burst duration as a function of cell length, measured using the TrackMate particle tracking  
899 algorithm on TIRF microscopy movies. The slopes of the linear regressions are not  
900 significantly different ( $p=0.8352$ ,  $R^2_{2\%}=0.3$ ,  $R^2_{0.03\%}=0.002$ ), and the values of the  
901 intercepts of the regressions are not significantly different ( $p=0.5392$ ). For (B-C),  $b_1$   
902 denotes slope and  $b_0$  denotes the Y-intercept. **(D)** Western blot of Wee1 in wild-type,  
903 *pom1* $\Delta$ , and *cdr2* $\Delta$  cells grown in high (2%) or low (0.03%) glucose media showing  
904 phosphorylation dependent band-shifts. Whole cell extracts were separated by SDS-  
905 PAGE, and blots were probed with an  $\alpha$ -Wee1 antibody.

906

907

908 **Figure 9: A model for the glucose-modulated control of Wee1 bursting by Pom1 and**  
909 **Cdr2.** See text for discussion.

910

911 **Supplemental Figure S1 (Figure 1): Analysis of the Pom1 gradient by confocal**  
912 **microscopy. (A)** Similar to TIRF microscopy, at middle-cell focal planes, discrete Pom1-  
913 mNeonGreen puncta are apparent at the lateral cell cortex of cells in individual frames  
914 (200ms) of spinning-disc microscopy movies. Scale bar 1 $\mu$ m. **(B)** Individual Pom1 puncta  
915 become averaged out in a projection of the entire continuous spinning-disc confocal  
916 microscopy movie. Sum projection of a continuous 15s time-lapse acquisition of 200ms  
917 exposures. **(C)** A line scan along the cell-perimeter in the direction indicated by the arrow  
918 of the single time-point micrograph of the cell in (A) reveals that Pom1 puncta form a noisy  
919 concentration gradient that begins at the cell tip and decays toward the cell middle. **(D)**  
920 The same line scan as in panel C, but of the time-lapse sum projection of the cell in panel  
921 B. This plot demonstrates that time-averaging of Pom1 puncta smoothens the  
922 concentration gradient. **(E)** Spinning-disc confocal micrographs of single 200ms  
923 acquisitions and **(F)** sum-projections of time lapse movies as in panels A and B  
924 respectively, but using a top-focal plane. **(G-H)** Line scan using a straight line across the  
925 long axis of the cell indicated by the arrow head on both the single time-point (G) and sum  
926 projection (H) of a 15s continuous time-lapse movie. **(I-J)** Representative images of  
927 Airyscan super-resolution micrographs of Pom1-mNeonGreen at either the cell tips (I) or  
928 cell side (J). Images are sum projections of sequential five-frame Z-stacks spaced 0.17 $\mu$ m

929 apart, positioned to include all detected cortical Pom1-mNeonGreen signal. Scale bar,  
930 1 $\mu$ m. **(K)** Fluorescence intensities of all single puncta resolved in Airyscan images as in  
931 panels I-J. Data points represent individual puncta values, error bars are the mean and  
932 standard deviation.

933  
934 Supplemental Figure S2 (Figure 2): Controls and supporting *in vitro* analysis of Pom1  
935 **puncta. (A)** Fluorescence intensity trace of a single Pom1 puncta binding to the cell  
936 cortex, measured by high speed TIRF microscopy of a cell expressing Pom1-mNG (~50  
937 frames per second with continuous acquisition). Rapid intensity changes indicating  
938 binding and unbinding are indicated by green upward and magenta downward pointing  
939 arrows respectively. **(B)** Size standards for velocity sucrose gradients, as in main Figure  
940 2C-E. Data are quantified from single Coomassie-stained gels, or using  
941 spectrophotometry data. **(C)** Plot of S-value versus sedimentation pattern. Line is linear  
942 regression of the three size standards, with the S-value for Pom1 peaks interpolated. **(D)**  
943 Quantification and comparison of binding duration of either wild-type or kinase-dead  
944 Pom1-mNG to supported lipid bilayers in TIRF microscopy movies ( $***p < 0.0001$ ).  
945 Statistical significance was tested with a Student's T-test. **(E)** FRAP analysis of supported  
946 lipid bilayers. Upper panel: A circular ROI (teal dashed line) was used to bleach  
947 fluorescent PE in the bilayers. Lower panel: Kymograph at white dashed line in upper  
948 panel of fluorescence recovery as monitored by TIRF microscopy, indicating fluidity.

949  
950 Supplemental Figure S3 (Figure 3): Representative single-cell data used to compute  
951 **mean cellular values in Figure 3. (A)** Quantification of binding duration of individual  
952 Pom1-mNG puncta at the tips or sides of representative wild-type, *tea1* $\Delta$  or *tea4* $\Delta$  cells,  
953 measured by TIRF microscopy. **(B)** Quantification of total displacement of individual  
954 Pom1-mNG puncta at the tips or sides of representative wild-type, *tea1* $\Delta$  or *tea4* $\Delta$  cells,  
955 measured by TIRF microscopy. For A-B, line and error represent single cell mean and  
956 standard deviation.

957  
958 Supplemental Figure S4 (Figure 4): Supporting analysis of Cdr2 nodes and Pom1  
959 **puncta at the medial cell cortex. (A)** Comparison of Pom1 puncta binding frequency on



960 the cell sides of wild-type and *cdr2Δ* cells (n.s.,  $p=0.1076$ ). **(B)** Comparison of Pom1  
961 puncta binding duration on the cell sides of wild-type and *cdr2Δ* cells (n.s.,  $p=0.371$ ). **(C)**  
962 Comparison of Pom1 puncta displacement on the cell sides of wild-type and *cdr2Δ* cells  
963 (n.s.,  $p=0.8191$ ). In A-C, significance was tested using a Student's T-test. **(D)** Schematic  
964 and quantification of Pom1 concentration at the lateral cell cortex measured by confocal  
965 microscopy, using 2 $\mu$ m line scans at the cell middle from images such as Figure 5A. The  
966 slope of the linear regression is negative, but not significantly non-zero ( $p=0.2603$ ,  
967  $R^2=0.03$ ). **(E)** Plot of the number of colocalized structures counted in a middle cell 2x2 $\mu$ m  
968 ROI as a function of cell size. The slope of the linear regression is significantly non-zero  
969 ( $p=0.0006$ ,  $R^2=0.3$ ). **(F)** Plot of free, non-colocalized Cdr2 nodes (blue circles) and Pom1  
970 puncta (red squares). The slope of the linear regression of #Pom1 puncta versus cell  
971 length is negative, and significantly non-zero ( $p=0.001$ ,  $R^2=0.27$ ). The slope of the linear  
972 regression of #Cdr2 nodes versus cell length is positive, and significantly non-zero  
973 ( $p=0.021$ ,  $R^2=0.15$ ).

974  
975 Supplemental Figure S5 (Figure 5): *In vitro* analysis of Pom1 activity in *tea1Δ* cells.

976 **(A)** Western blot of an *in vitro* thiophosphate kinase assay to test Pom1  
977 autophosphorylation activity in *pom1-3HA*, *pom1-AS-3HA*, and *pom1-AS-3HA tea1Δ*  
978 cells. Blots were probed with an  $\alpha$ -thiophosphate antibody. Only analog-sensitive (AS)  
979 alleles can use ATP $\gamma$ S to thio-phosphorylate substrates. **(B)** Comparison of western blot  
980 band intensities from four replicate gels, derived from two separate experiments as in  
981 panel A. Statistical significance was tested using a paired T-test between *Pom1-AS-3HA*  
982 and *Pom1-AS-3HA tea1Δ* cells (\*,  $p=0.02$ ). **(C)** Western blot of an *in vitro* thiophosphate  
983 kinase assay to measure phosphorylation of purified Cdr2 by Pom1 in *pom1-3HA*, *pom1-*  
984 *AS-3HA*, and *pom1-AS-3HA tea1Δ* cells. Blots were probed with an anti-thiophosphate  
985 antibody. Excess Pom1-3HA was used in lanes 1 and 3 to ensure absence of signal in  
986 negative controls lacking the analog-sensitive mutation. Cdr2(712-775) is a fragment that  
987 contains known Pom1 phosphorylation sites. **(D)** Western blot of the Pom1 substrate  
988 Rga7-3HA in wild-type, *tea1Δ*, and *pom1Δ* cells. Whole-cell extracts were separated by  
989 SDS-PAGE, and probed with  $\alpha$ -HA antibodies. The upper band represents a Pom1-  
990 dependent phospho-isoform. **(E)** Comparison of band intensities from four replicate gels

991 as in (D), expressed as the ratio of the grey-value of the top band/bottom band. Line and  
992 error are mean and standard deviation. Statistical significance was tested using a one-  
993 way ANOVA and Tukey's multiple comparisons test (WT vs *tea1* $\Delta$ , \*\*\* $p=0.003$ , WT vs  
994 *pom1* $\Delta$ , \*\*\*\* $p<0.0001$ , *tea1* $\Delta$  vs *pom1* $\Delta$ , \*\*\*\* $p<0.0001$ ).

995

996 Supplemental Figure S6 (Figure 5): Control of Pom1 concentration at the cell side.

997 **(A)** Localization of Pom1-mNG in wild-type, *tea1* $\Delta$ , and *pom1-KD* (kinase-dead) cells at  
998 the indicated concentration of glucose. Images are confocal micrographs taken at a  
999 middle cell focal plane. Scale bar, 5 $\mu$ m. **(B)** Quantification of Pom1 concentration along  
1000 2 $\mu$ m line scans as in figure S4D, measured using images as in panel A. The means of  
1001 each column are significantly different from every other column ( $p<0.005$ ). Statistical  
1002 significance was tested using a one-way ANOVA and Tukey's multiple comparison's test.  
1003 **(C)** Plot of Pom1 concentration at the cell side as a function of glucose concentration in  
1004 the growth media. Data were fit to an exponential curve showing a negative sinusoidal  
1005 relationship reaching half saturation at  $\sim 0.05\%$  glucose. The concentration of Pom1-mNG  
1006 at the lateral cell cortex in a *tea1* $\Delta$  mutant was fit to this curve, and is the approximate  
1007 equivalent of wild-type cells grown in 0.03% Glucose. Line and error are mean and  
1008 standard deviation. (D) Localization of Tea4-mNG in wild-type or *tea1* $\Delta$  cells grown in the  
1009 indicated concentration of glucose for one hour. Images are confocal micrographs taken  
1010 at middle cell focal planes. Arrows point to lateral puncta of Tea4-mNG. Scale bar, 5 $\mu$ m.

1011

1012 Supplemental Figure S7 (Figure 6): Redistribution of Pom1 puncta to the lateral

1013 **cortex disrupts Cdr2 nodes during glucose restriction, supporting data.** **(A)** Analysis  
1014 of Pom1 and Cdr2 redistribution by spinning-disc confocal microscopy, as in (Kelkar and  
1015 Martin, 2015). Images are confocal micrographs of cells co-expressing Pom1-tdTomato  
1016 and Cdr2-mNG in high (2%) or low (0.03%) glucose media. Scale bar, 5 $\mu$ m. **(B)** Cortical  
1017 fluorescence intensity of Cdr2 and Pom1 was measured using line scans drawn around  
1018 the circumference of the representative cell marked with an arrowhead in the 2% glucose  
1019 portion of panel A. **(C)** Cortical fluorescence intensity of Cdr2 and Pom1 was measured  
1020 using line scans drawn around the circumference of the representative cell marked with  
1021 an arrowhead in the 0.03% glucose portion of panel A.

1022  
1023 Supplemental Figure S8 (Figure 8): Re-plotting of data from Main Figure 8 for  
1024 **additional comparison. (A)** Plot of the frequency of Wee1 bursts as a function of cell  
1025 length in wild-type cells grown in high (2%) glucose (blue circles) and low glucose (red  
1026 squares), and kinase-dead *cdr2(E177A)* mutant cells grown in 2% glucose (green  
1027 triangles). Measurements were made using the TrackMate particle tracking algorithm on  
1028 TIRF microscopy movies. The slopes of the linear regressions are not significantly  
1029 different ( $p=0.7651$ ,  $R^2_{2\%}=0.5$ ,  $R^2_{0.03\%}=0.51$ ,  $R^2_{Cdr2(E177A)}=0.51$ ) and the elevations of the  
1030 regressions are also not significantly different ( $p=0.4397$ ). **(B)** Plot of Wee1 burst duration  
1031 as a function of cell length in wild-type cells grown in low glucose (red squares) and  
1032 kinase-dead *cdr2(E177A)* mutant cells grown in 2% glucose (green triangles).  
1033 Measurements were made using the Trackmate particle tracking algorithm on TIRF  
1034 microscopy movies. The slopes of the linear regressions are not significantly different  
1035 ( $p=0.8048$ ,  $R^2_{0.03\%}=0.05$ ,  $R^2_{Cdr2(E177A)}=0.2$ ) and the elevations of the regressions are also  
1036 not significantly different ( $p=0.8048$ ).

1037  
1038 Supplemental Table S1: Fission yeast strains used in this study.

1039

## 1040 **Acknowledgements:**

1041 We thank members of the Moseley lab and Erik Griffin for comments on the manuscript,  
1042 as well as B. Wickner and C. Barlowe and the Norris Cotton Cancer Center Molecular  
1043 Interactions & Imaging Core at Dartmouth for sharing equipment. A. Lavanway, Z.  
1044 Svindrych and the Life Sciences Light Microscopy Facility for assistance with microscopy.  
1045 A. Orr for assistance with ultracentrifugation. Youjun Wu for recombinant Pom1 proteins.  
1046 This work was supported by grants from the American Cancer Society (RSG-15-140-01-  
1047 CCG) and the NIH (R01 GM099774) to J.B.M; and an NIH Training Grant  
1048 (T32GM008704) to C.A.H.A. Shared imaging resources were supported by grants from  
1049 the NIH (1S10OD018046 and P20GM113132).

1050

1051

1052

1053 **References:**

1054 Akamatsu, M., Berro, J., Pu, K.-M., Tebbs, I.R., and Pollard, T.D. (2014). Cytokinetic  
1055 nodes in fission yeast arise from two distinct types of nodes that merge during interphase.  
1056 *J Cell Biol* 204, 977–988.

1057 Akamatsu, M., Lin, Y., Bewersdorf, J., and Pollard, T.D. (2017). Analysis of interphase  
1058 node proteins in fission yeast by quantitative and superresolution fluorescence  
1059 microscopy. *Mol. Biol. Cell* 28, 3203–3214.

1060 Alberghina, L., Höfer, T., and Vanoni, M. (2009). Molecular networks and system-level  
1061 properties. *J. Biotechnol.* 144, 224–233.

1062 Aligue, R., Wu, L., and Russell, P. (1997). Regulation of *Schizosaccharomyces pombe*  
1063 Wee1 Tyrosine Kinase. *J. Biol. Chem.* 272, 13320–13325.

1064 Allard, C.A.H., Opalko, H.E., Liu, K.-W., Medoh, U., and Moseley, J.B. (2018). Cell size–  
1065 dependent regulation of Wee1 localization by Cdr2 cortical nodes. *J Cell Biol* 217, 1589–  
1066 1599.

1067 Bähler, J., and Nurse, P. (2001). Fission yeast Pom1p kinase activity is cell cycle  
1068 regulated and essential for cellular symmetry during growth and division. *EMBO J.* 20,  
1069 1064–1073.

1070 Bähler, J., and Pringle, J.R. (1998). Pom1p, a fission yeast protein kinase that provides  
1071 positional information for both polarized growth and cytokinesis. *Genes Dev.* 12, 1356–  
1072 1370.

1073 Bähler, J., Wu, J.-Q., Longtine, M.S., Shah, N.G., Iii, A.M., Steever, A.B., Wach, A.,  
1074 Philippsen, P., and Pringle, J.R. (1998). Heterologous modules for efficient and versatile  
1075 PCR-based gene targeting in *Schizosaccharomyces pombe*. *Yeast* 14, 943–951.

1076 Bhatia, P., Hachet, O., Hersch, M., Rincon, S.A., Berthelot-Grosjean, M., Dalessi, S.,  
1077 Basterra, L., Bergmann, S., Paoletti, A., and Martin, S.G. (2014). Distinct levels in Pom1  
1078 gradients limit Cdr2 activity and localization to time and position division. *Cell Cycle*  
1079 *Georget. Tex* 13, 538–552.

1080 Bray, D., Levin, M.D., and Morton-Firth, C.J. (1998). Receptor clustering as a cellular  
1081 mechanism to control sensitivity. *Nature* 393, 85–88.

1082 Breeding, C.S., Hudson, J., Balasubramanian, M.K., Hemmingsen, S.M., Young, P.G.,  
1083 and Gould, K.L. (1998). The *cdr2(+)* gene encodes a regulator of G2/M progression and  
1084 cytokinesis in *Schizosaccharomyces pombe*. *Mol. Biol. Cell* 9, 3399–3415.

1085 Chang, F., and Martin, S.G. (2009). Shaping Fission Yeast with Microtubules. *Cold Spring*  
1086 *Harb. Perspect. Biol.* 1, a001347.

- 1087 Deng, L., and Moseley, J.B. (2013). Compartmentalized nodes control mitotic entry  
1088 signaling in fission yeast. *Mol. Biol. Cell* 24, 1872–1881.
- 1089 Deng, L., Baldissard, S., Kettenbach, A.N., Gerber, S.A., and Moseley, J.B. (2014).  
1090 Dueling Kinases Regulate Cell Size at Division through the SAD Kinase Cdr2. *Curr. Biol.*  
1091 24, 428–433.
- 1092 Dickinson, D.J., Schwager, F., Pintard, L., Gotta, M., and Goldstein, B. (2017). A Single-  
1093 Cell Biochemistry Approach Reveals PAR Complex Dynamics during Cell Polarization.  
1094 *Dev. Cell* 42, 416-434.e11.
- 1095 Dodgson, J., Chessel, A., Yamamoto, M., Vaggi, F., Cox, S., Rosten, E., Albrecht, D.,  
1096 Geymonat, M., Csikasz-Nagy, A., Sato, M., et al. (2013). Spatial segregation of polarity  
1097 factors into distinct cortical clusters is required for cell polarity control. *Nat. Commun.* 4,  
1098 1834.
- 1099 Douglass, A.D., and Vale, R.D. (2005). Single-molecule microscopy reveals plasma  
1100 membrane microdomains created by protein-protein networks that exclude or trap  
1101 signaling molecules in T cells. *Cell* 121, 937–950.
- 1102 Duke, T.A., and Bray, D. (1999). Heightened sensitivity of a lattice of membrane  
1103 receptors. *Proc. Natl. Acad. Sci. U. S. A.* 96, 10104–10108.
- 1104 Facchetti, G., Knapp, B., Flor-Parra, I., Chang, F., and Howard, M. (2019).  
1105 Reprogramming Cdr2-Dependent Geometry-Based Cell Size Control in Fission Yeast.  
1106 *Curr. Biol.* 29, 350-358.e4.
- 1107 Falke, J.J. (2002). Cooperativity between bacterial chemotaxis receptors. *Proc. Natl.*  
1108 *Acad. Sci. U. S. A.* 99, 6530–6532.
- 1109 Fantes, P., and Nurse, P. (1977). Control of cell size at division in fission yeast by a  
1110 growth-modulated size control over nuclear division. *Exp. Cell Res.* 107, 377–386.
- 1111 Gautier, J., Solomon, M.J., Booher, R.N., Bazan, J.F., and Kirschner, M.W. (1991). *cdc25*  
1112 is a specific tyrosine phosphatase that directly activates p34cdc2. *Cell* 67, 197–211.
- 1113 Ginzberg, M.B., Kafri, R., and Kirschner, M. (2015). Cell biology. On being the right (cell)  
1114 size. *Science* 348, 1245075.
- 1115 Gould, K.L., and Nurse, P. (1989). Tyrosine phosphorylation of the fission yeast *cdc2* +  
1116 protein kinase regulates entry into mitosis. *Nature* 342, 39.
- 1117 Gronnier, J., Crowet, J.-M., Habenstein, B., Nasir, M.N., Bayle, V., Hosy, E., Platre, M.P.,  
1118 Gouguet, P., Raffaele, S., Martinez, D., et al. (2017). Structural basis for plant plasma  
1119 membrane protein dynamics and organization into functional nanodomains. *ELife* 6.
- 1120 Gu, Y., and Oliferenko, S. (2019). Cellular geometry scaling ensures robust division site  
1121 positioning. *Nat. Commun.* 10, 268.

- 1122 Guzmán-Vendrell, M., Rincon, S.A., Dingli, F., Loew, D., and Paoletti, A. (2015).  
1123 Molecular control of the Wee1 regulatory pathway by the SAD kinase Cdr2. *J. Cell Sci.*  
1124 *128*, 2842–2853.
- 1125 Hachet, O., Berthelot-Grosjean, M., Kokkoris, K., Vincenzetti, V., Moosbrugger, J., and  
1126 Martin, S.G. (2011). A phosphorylation cycle shapes gradients of the DYRK family kinase  
1127 Pom1 at the plasma membrane. *Cell* *145*, 1116–1128.
- 1128 Harashima, H., Dissmeyer, N., and Schnittger, A. (2013). Cell cycle control across the  
1129 eukaryotic kingdom. *Trends Cell Biol.* *23*, 345–356.
- 1130 Haupt, A., and Minc, N. (2017). Gradients of phosphatidylserine contribute to plasma  
1131 membrane charge localization and cell polarity in fission yeast. *Mol. Biol. Cell* *28*, 210–  
1132 220.
- 1133 Hersch, M., Hachet, O., Dalessi, S., Ullal, P., Bhatia, P., Bergmann, S., and Martin, S.G.  
1134 (2015). Pom1 gradient buffering through intermolecular auto-phosphorylation. *Mol. Syst.*  
1135 *Biol.* *11*, 818.
- 1136 Jorgensen, P., and Tyers, M. (2004). How Cells Coordinate Growth and Division. *Curr.*  
1137 *Biol.* *14*, R1014–R1027.
- 1138 Kalay, Z., Fujiwara, T.K., and Kusumi, A. (2012). Confining domains lead to reaction  
1139 bursts: reaction kinetics in the plasma membrane. *PLoS One* *7*, e32948.
- 1140 Kanoh, J., and Russell, P. (1998). The Protein Kinase Cdr2, Related to Nim1/Cdr1 Mitotic  
1141 Inducer, Regulates the Onset of Mitosis in Fission Yeast. *Mol. Biol. Cell* *9*, 3321–3334.
- 1142 Keifenheim, D., Sun, X.-M., D'Souza, E., Ohira, M.J., Magner, M., Mayhew, M.B.,  
1143 Marguerat, S., and Rhind, N. (2017). Size-Dependent Expression of the Mitotic Activator  
1144 Cdc25 Suggests a Mechanism of Size Control in Fission Yeast. *Curr. Biol.* *CB* *27*, 1491-  
1145 1497.e4.
- 1146 Kelkar, M., and Martin, S.G. (2015). PKA antagonizes CLASP-dependent microtubule  
1147 stabilization to re-localize Pom1 and buffer cell size upon glucose limitation. *Nat.*  
1148 *Commun.* *6*, 8445.
- 1149 Kettenbach, A.N., Deng, L., Wu, Y., Baldissard, S., Adamo, M.E., Gerber, S.A., and  
1150 Moseley, J.B. (2015). Quantitative phosphoproteomics reveals pathways for coordination  
1151 of cell growth and division by the conserved fission yeast kinase pom1. *Mol. Cell.*  
1152 *Proteomics MCP* *14*, 1275–1287.
- 1153 Kumagai, A., and Dunphy, W.G. (1991). The cdc25 protein controls tyrosine  
1154 dephosphorylation of the cdc2 protein in a cell-free system. *Cell* *64*, 903–914.
- 1155 Liu, W., Wang, H., and Xu, C. (2016). Antigen Receptor Nanoclusters: Small Units with  
1156 Big Functions. *Trends Immunol.* *37*, 680–689.

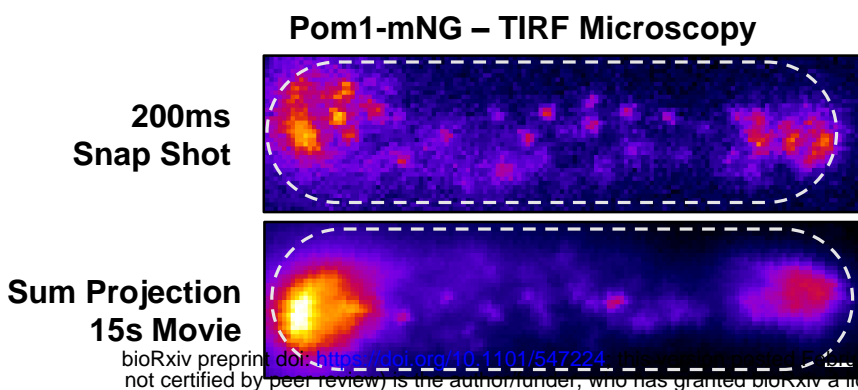
- 1157 Lloyd, A.C. (2013). The Regulation of Cell Size. *Cell* *154*, 1194–1205.
- 1158 Lucena, R., Alcaide-Gavilán, M., Anastasia, S.D., and Kellogg, D.R. (2017). Wee1 and  
1159 Cdc25 are controlled by conserved PP2A-dependent mechanisms in fission yeast. *Cell*  
1160 *Cycle* *16*, 428–435.
- 1161 Maity, P.C., Blount, A., Jumaa, H., Ronneberger, O., Lillemeier, B.F., and Reth, M. (2015).  
1162 B cell antigen receptors of the IgM and IgD classes are clustered in different protein  
1163 islands that are altered during B cell activation. *Sci. Signal.* *8*, ra93.
- 1164 Makushok, T., Alves, P., Huisman, S.M., Kijowski, A.R., and Brunner, D. (2016). Sterol-  
1165 Rich Membrane Domains Define Fission Yeast Cell Polarity. *Cell* *165*, 1182–1196.
- 1166 Martin, S.G., and Berthelot-Grosjean, M. (2009). Polar gradients of the DYRK-family  
1167 kinase Pom1 couple cell length with the cell cycle. *Nature* *459*, 852–856.
- 1168 Masuda, H., Fong, C.S., Ohtsuki, C., Haraguchi, T., and Hiraoka, Y. (2011).  
1169 Spatiotemporal regulations of Wee1 at the G2/M transition. *Mol. Biol. Cell* *22*, 555–569.
- 1170 Moreno, S., Hayles, J., and Nurse, P. (1989). Regulation of p34cdc2 protein kinase during  
1171 mitosis. *Cell* *58*, 361–372.
- 1172 Moreno, S., Nurse, P., and Russell, P. (1990). Regulation of mitosis by cyclic  
1173 accumulation of p80cdc25 mitotic inducer in fission yeast. *Nature* *344*, 549–552.
- 1174 Moreno, S., Klar, A., and Nurse, P. (1991). Molecular genetic analysis of fission yeast  
1175 *Schizosaccharomyces pombe*. *Methods Enzymol.* *194*, 795–823.
- 1176 Morrell, J.L., Nichols, C.B., and Gould, K.L. (2004). The GIN4 family kinase, Cdr2p, acts  
1177 independently of septins in fission yeast. *J. Cell Sci.* *117*, 5293–5302.
- 1178 Moseley, J.B., Mayeux, A., Paoletti, A., and Nurse, P. (2009). A spatial gradient  
1179 coordinates cell size and mitotic entry in fission yeast. *Nature* *459*, 857–860.
- 1180 Munro, E. (2017). Protein Clustering Shapes Polarity Protein Gradients. *Dev. Cell* *42*,  
1181 309–311.
- 1182 Neumann, F.R., and Nurse, P. (2007). Nuclear size control in fission yeast. *J. Cell Biol.*  
1183 *179*, 593–600.
- 1184 Opalko, H.E., and Moseley, J.B. (2017). Dynamic regulation of Cdr1 localization and  
1185 phosphorylation during osmotic stress. *J. Biol. Chem.* jbc.M117.793034.
- 1186 Pan, K.Z., Saunders, T.E., Flor-Parra, I., Howard, M., and Chang, F. (2014). Cortical  
1187 regulation of cell size by a sizer cdr2p. *ELife* *3*.

- 1188 Pluskal, T., Hayashi, T., Saitoh, S., Fujisawa, A., and Yanagida, M. (2011). Specific  
1189 biomarkers for stochastic division patterns and starvation-induced quiescence under  
1190 limited glucose levels in fission yeast. *FEBS J.* 278, 1299–1315.
- 1191 Rincon, S.A., Bhatia, P., Bicho, C., Guzman-Vendrell, M., Fraiser, V., Borek, W.E., Alves,  
1192 F. de L., Dingli, F., Loew, D., Rappsilber, J., et al. (2014). Pom1 regulates the assembly  
1193 of Cdr2–Mid1 cortical nodes for robust spatial control of cytokinesis. *J Cell Biol* 206, 61–  
1194 77.
- 1195 Rodriguez, J., Peglion, F., Martin, J., Hubatsch, L., Reich, J., Hirani, N., Gubieda, A.G.,  
1196 Roffey, J., Fernandes, A.R., St Johnston, D., et al. (2017). aPKC Cycles between  
1197 Functionally Distinct PAR Protein Assemblies to Drive Cell Polarity. *Dev. Cell* 42, 400–  
1198 415.e9.
- 1199 Russell, P., and Nurse, P. (1986). *cdc25+* functions as an inducer in the mitotic control of  
1200 fission yeast. *Cell* 45, 145–153.
- 1201 Russell, P., and Nurse, P. (1987). Negative regulation of mitosis by *wee1+*, a gene  
1202 encoding a protein kinase homolog. *Cell* 49, 559–567.
- 1203 Saunders, T.E., Pan, K.Z., Angel, A., Guan, Y., Shah, J.V., Howard, M., and Chang, F.  
1204 (2012). Noise reduction in the intracellular *pom1p* gradient by a dynamic clustering  
1205 mechanism. *Dev. Cell* 22, 558–572.
- 1206 Schmoller, K.M., Turner, J.J., Kõivomägi, M., and Skotheim, J.M. (2015). Dilution of the  
1207 cell cycle inhibitor *Whi5* controls budding-yeast cell size. *Nature* 526, 268–272.
- 1208 Shiozaki, K. (2009). Nutrition-Minded Cell Cycle. *Sci Signal* 2, pe74–pe74.
- 1209 Simanis, V., and Nurse, P. (1986). The cell cycle control gene *cdc2+* of fission yeast  
1210 encodes a protein kinase potentially regulated by phosphorylation. *Cell* 45, 261–268.
- 1211 Strausfeld, U., Labbé, J.C., Fesquet, D., Cavadore, J.C., Picard, A., Sadhu, K., Russell,  
1212 P., and Dorée, M. (1991). Dephosphorylation and activation of a p34cdc2/cyclin B  
1213 complex in vitro by human CDC25 protein. *Nature* 351, 242–245.
- 1214 Su, X., Ditlev, J.A., Hui, E., Xing, W., Banjade, S., Okrut, J., King, D.S., Taunton, J.,  
1215 Rosen, M.K., and Vale, R.D. (2016). Phase separation of signaling molecules promotes  
1216 T cell receptor signal transduction. *Science* 352, 595–599.
- 1217 Tinevez, J.-Y., Perry, N., Schindelin, J., Hoopes, G.M., Reynolds, G.D., Laplantine, E.,  
1218 Bednarek, S.Y., Shorte, S.L., and Eliceiri, K.W. (2017). TrackMate: An open and  
1219 extensible platform for single-particle tracking. *Methods* 115, 80–90.
- 1220 Wang, S.-C., Low, T.Y.F., Nishimura, Y., Gole, L., Yu, W., and Motegi, F. (2017). Cortical  
1221 forces and CDC-42 control clustering of PAR proteins for *Caenorhabditis elegans*  
1222 embryonic polarization. *Nat. Cell Biol.* 19, 988–995.

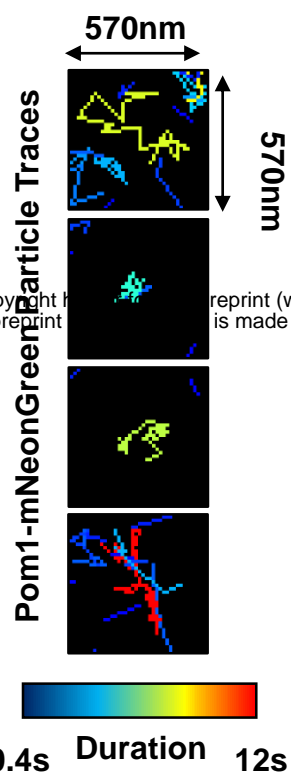


- 1223 Wood, E., and Nurse, P. (2013). Pom1 and cell size homeostasis in fission yeast. *Cell*  
1224 *Cycle Georget. Tex* 12, 3228–3236.
- 1225 Wu, L., and Russell, P. (1993). Nim1 kinase promotes mitosis by inactivating Wee1  
1226 tyrosine kinase. *Nature* 363, 738–741.
- 1227 Wu, L., Shiozaki, K., Aligue, R., and Russell, P. (1996). Spatial organization of the Nim1-  
1228 Wee1-Cdc2 mitotic control network in *Schizosaccharomyces pombe*. *Mol. Biol. Cell* 7,  
1229 1749–1758.
- 1230 Yanagida Mitsuhiro, Ikai Nobuyasu, Shimanuki Mizuki, and Sajiki Kenichi (2011). Nutrient  
1231 limitations alter cell division control and chromosome segregation through growth-related  
1232 kinases and phosphatases. *Philos. Trans. R. Soc. B Biol. Sci.* 366, 3508–3520.
- 1233 Young, P.G., and Fantes, P.A. (1987). *Schizosaccharomyces pombe* mutants affected in  
1234 their division response to starvation. *J. Cell Sci.* 88, 295–304.
- 1235 Zhou, Y., and Hancock, J.F. (2015). Ras nanoclusters: Versatile lipid-based signaling  
1236 platforms. *Biochim. Biophys. Acta* 1853, 841–849.
- 1237

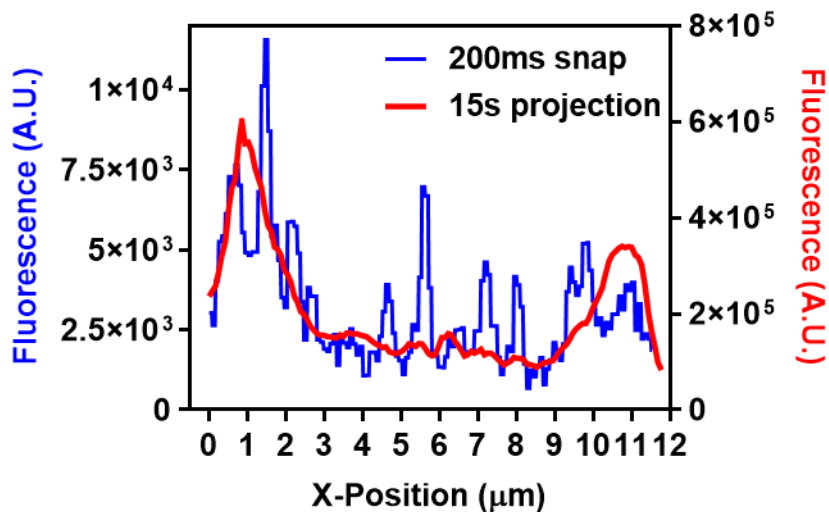
A.



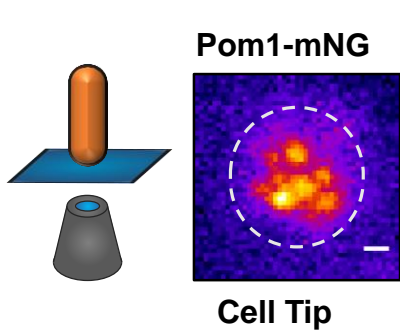
C.



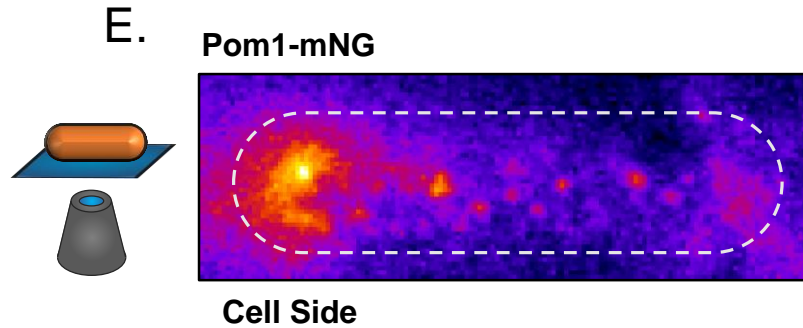
B.



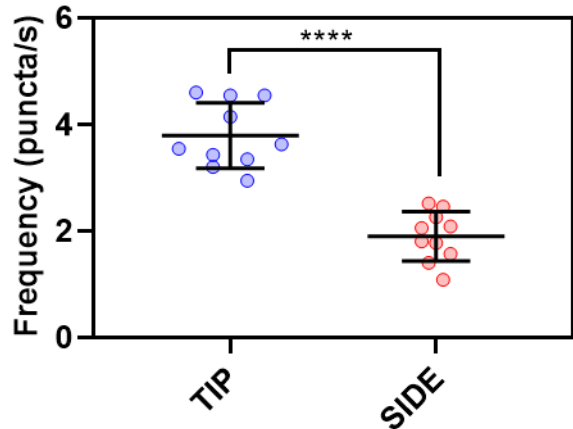
D.



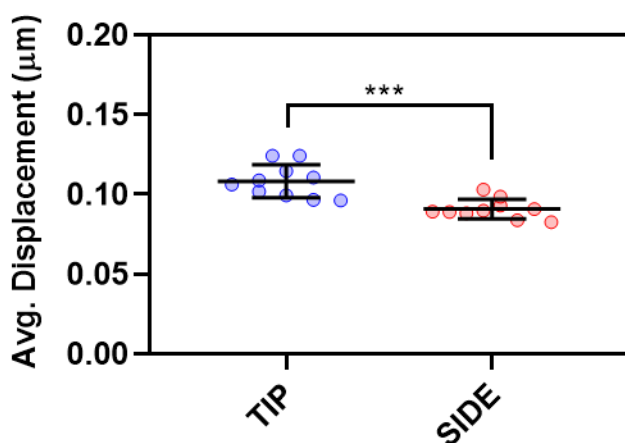
E.



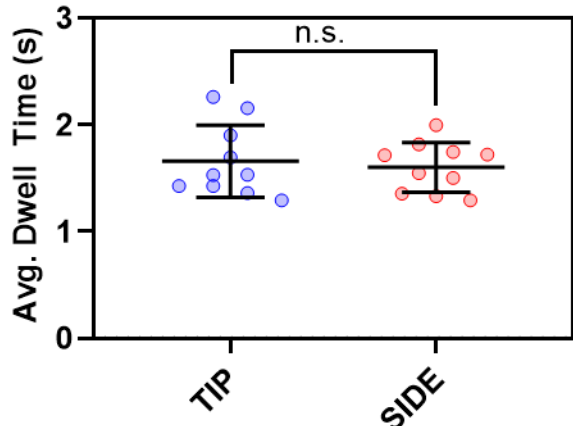
F.



G.



H.



I.

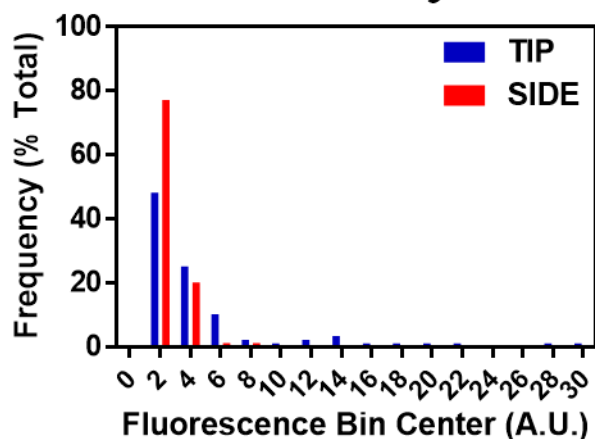
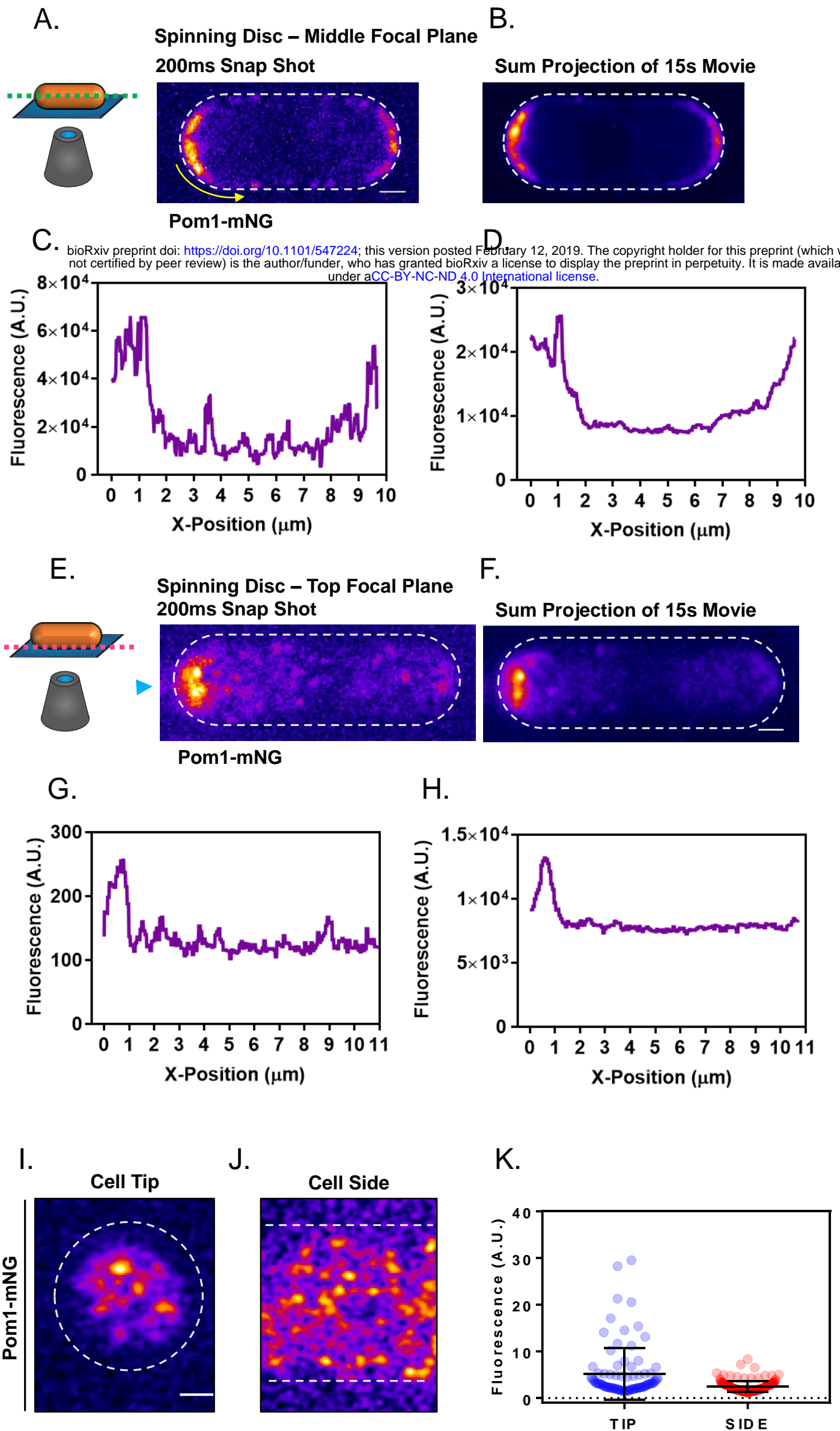
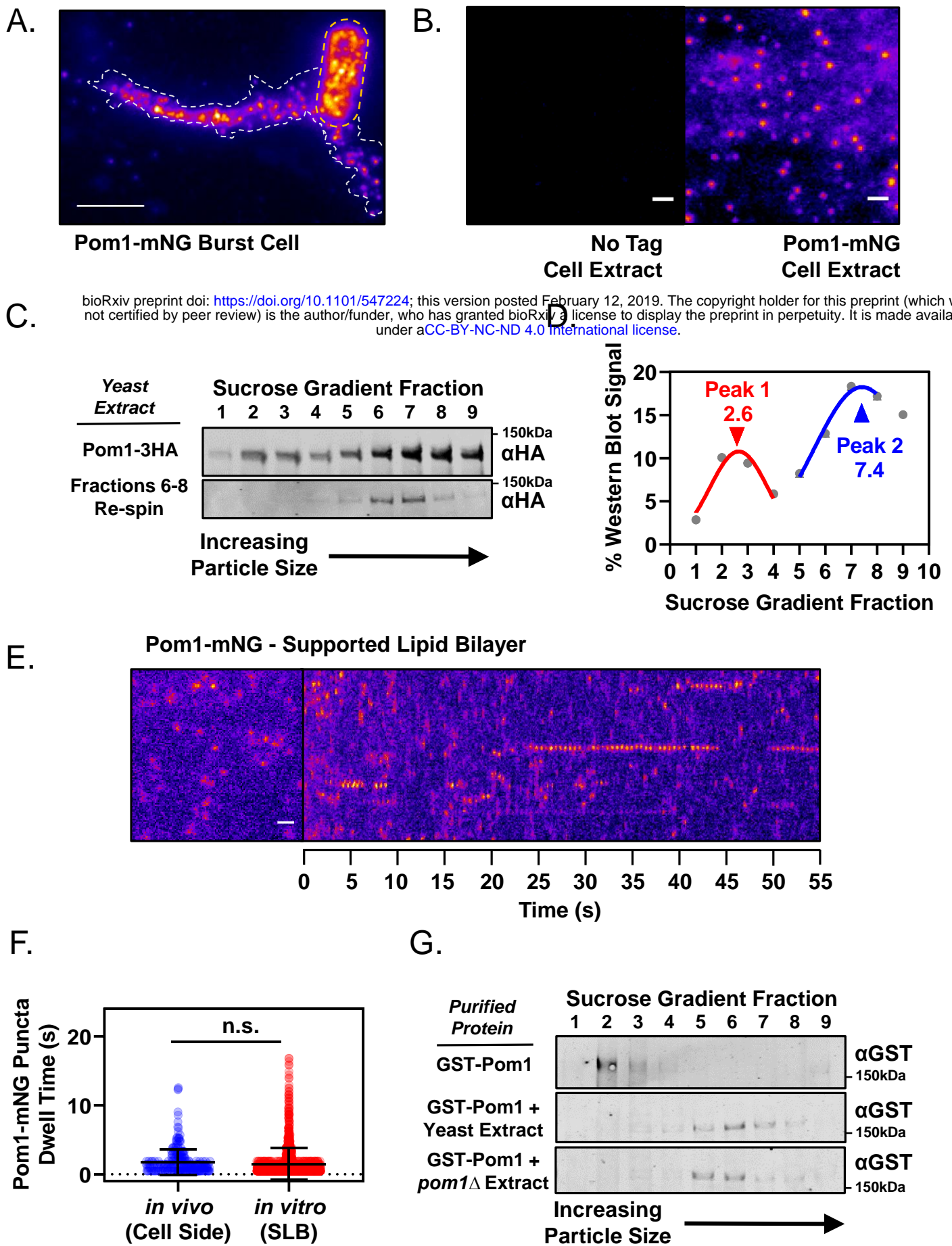
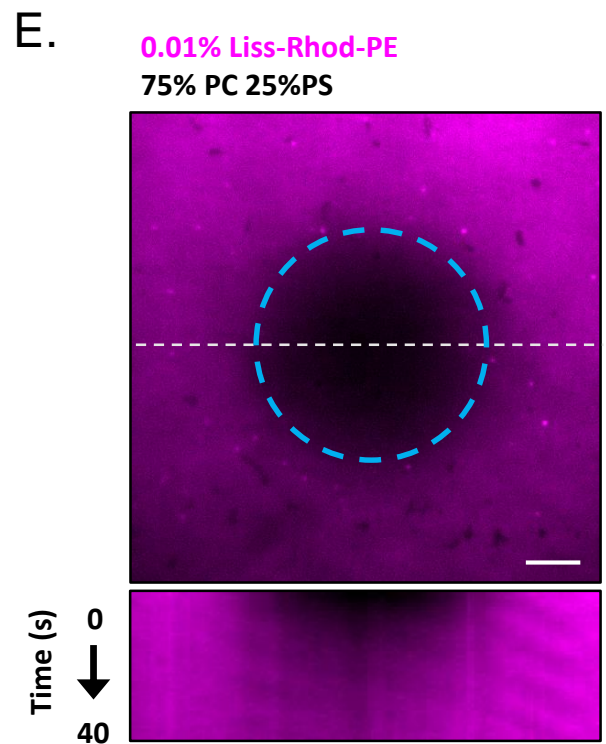
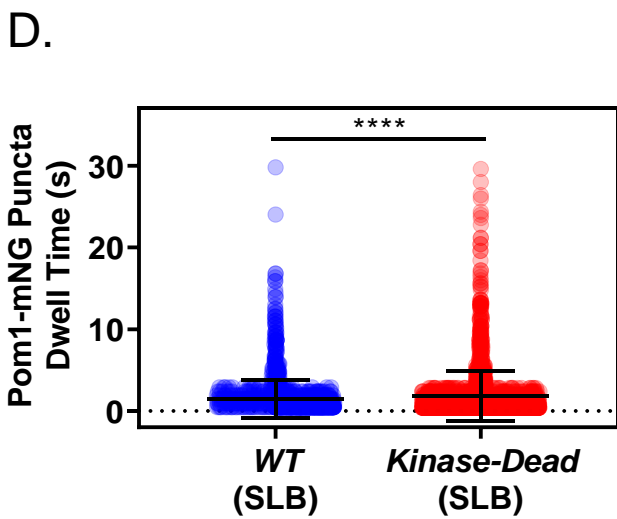
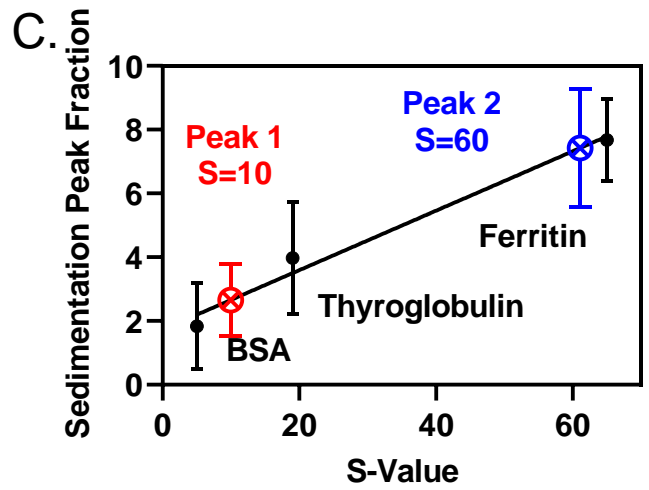
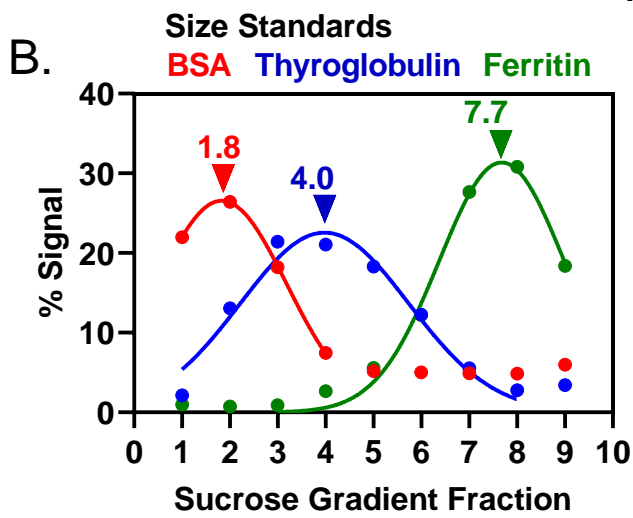
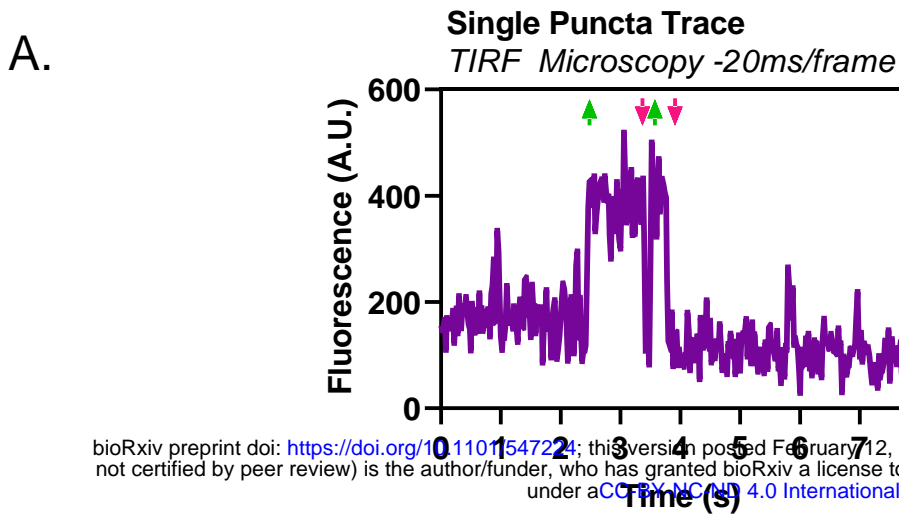


Figure 1

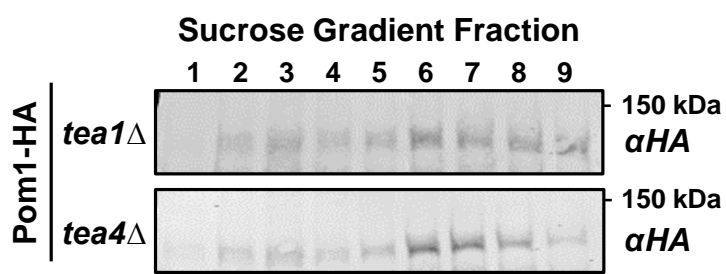


Supplemental Figure 1 in support of Figure 1



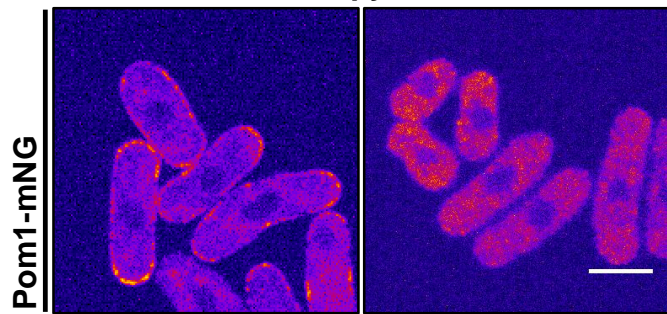


A.



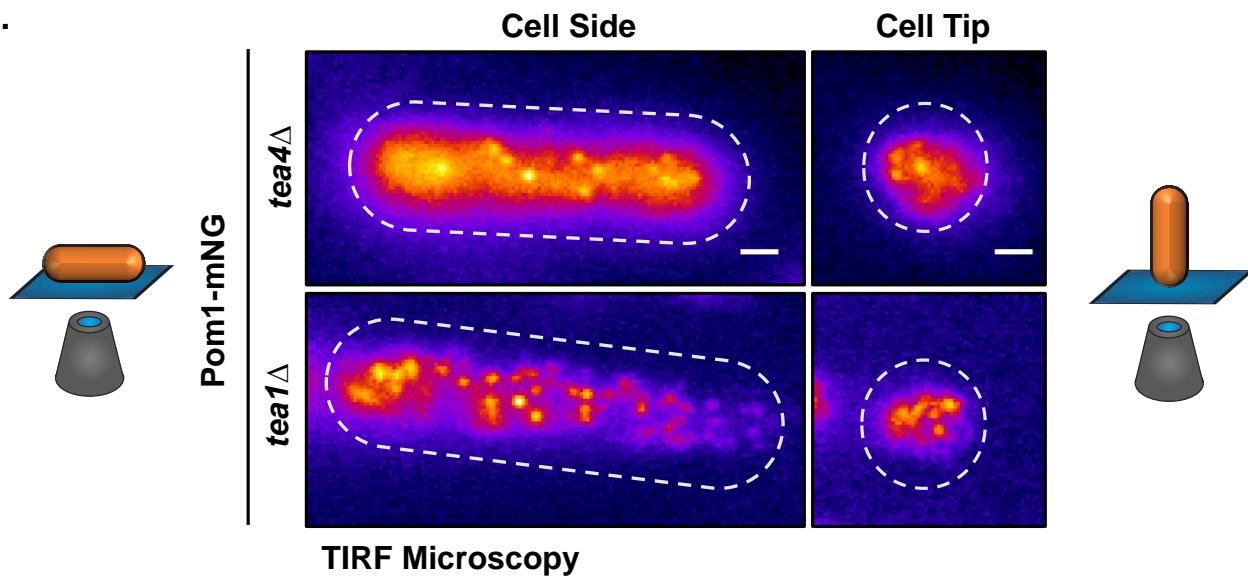
B.

Confocal Microscopy

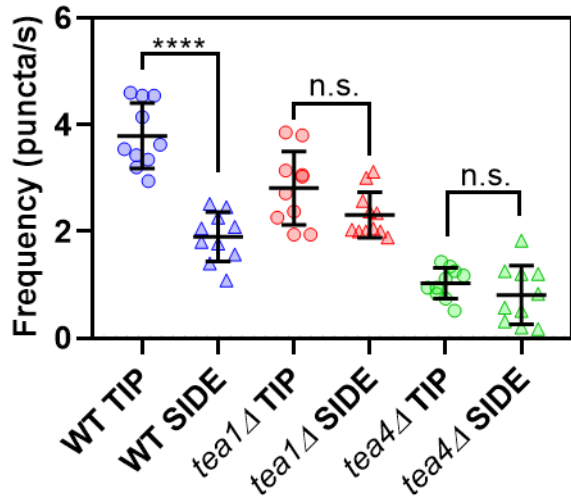


bioRxiv preprint doi: <https://doi.org/10.1101/547224>; this version posted February 12, 2019. The copyright holder for this preprint (which was not certified by peer review) is the author/funder, who has granted bioRxiv a license to display the preprint in perpetuity. It is made available under aCC-BY-NC-ND 4.0 International license.

C.



D.



E.

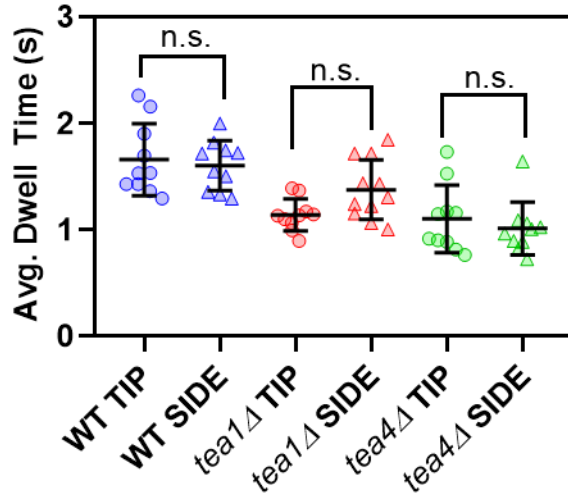
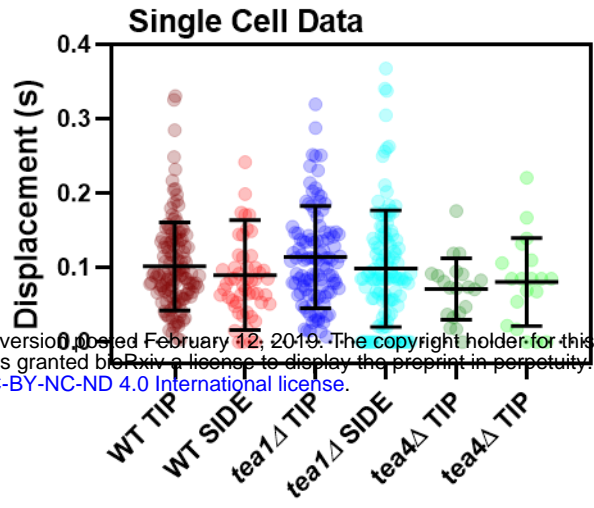
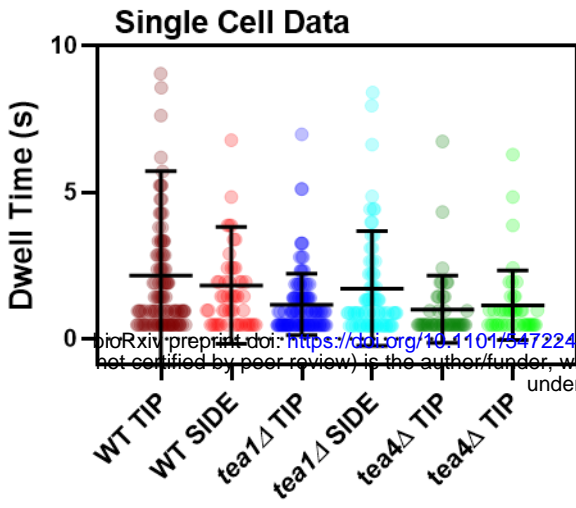


Figure 3

A.

B.



bioRxiv preprint doi: <https://doi.org/10.1101/317224>; this version posted February 12, 2019. The copyright holder for this preprint (which was not certified by peer review) is the author/funder, who has granted bioRxiv a license to display the preprint in perpetuity. It is made available under aCC-BY-NC-ND 4.0 International license.

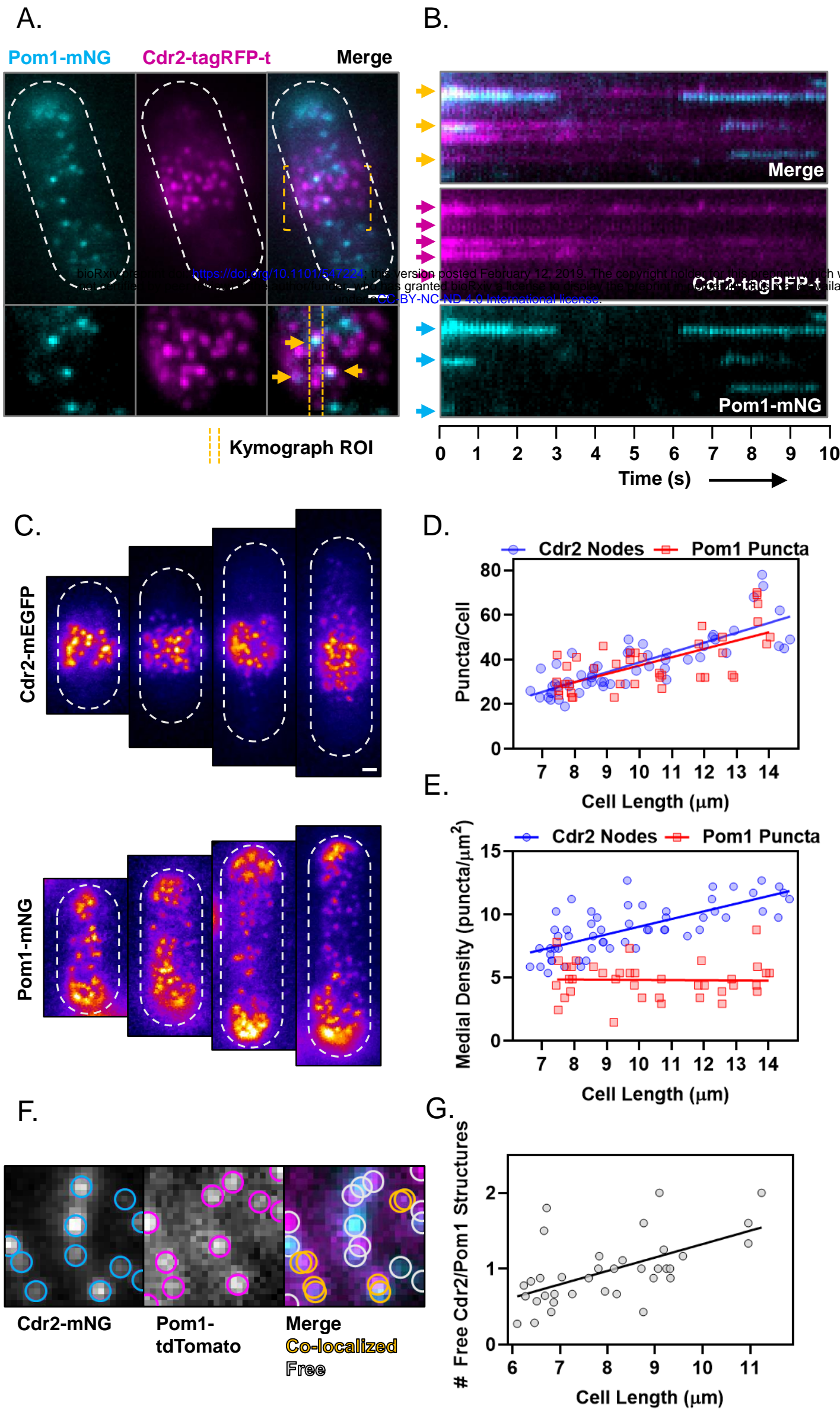
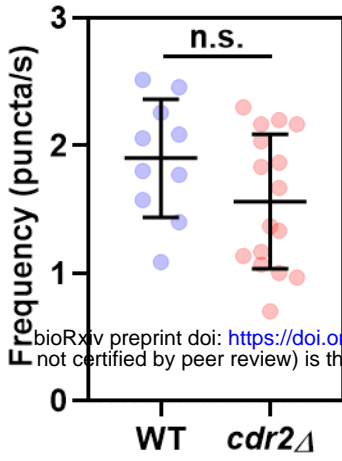


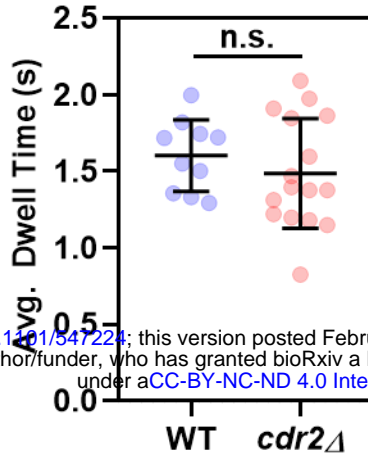
Figure 4



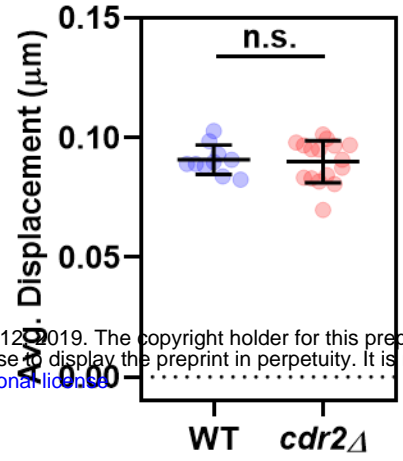
A.



B.

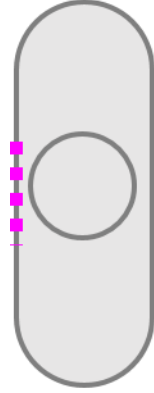


C.

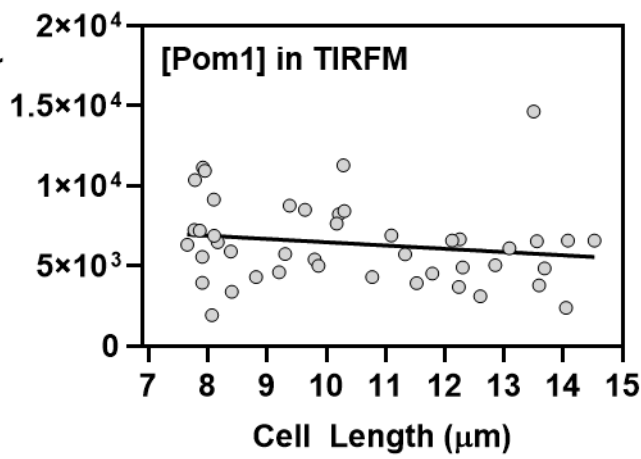


bioRxiv preprint doi: <https://doi.org/10.1101/347224>; this version posted February 12, 2019. The copyright holder for this preprint (which was not certified by peer review) is the author/funder, who has granted bioRxiv a license to display the preprint in perpetuity. It is made available under aCC-BY-NC-ND 4.0 International license.

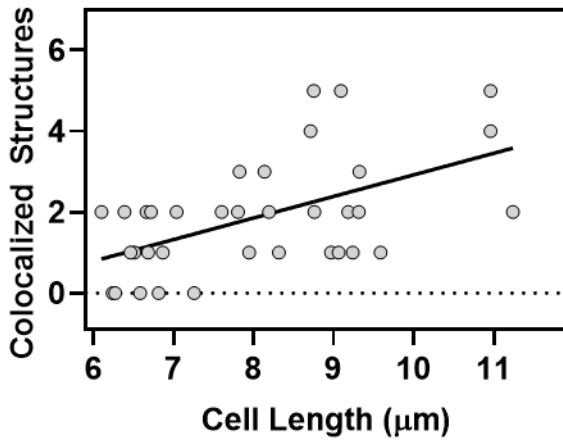
D.



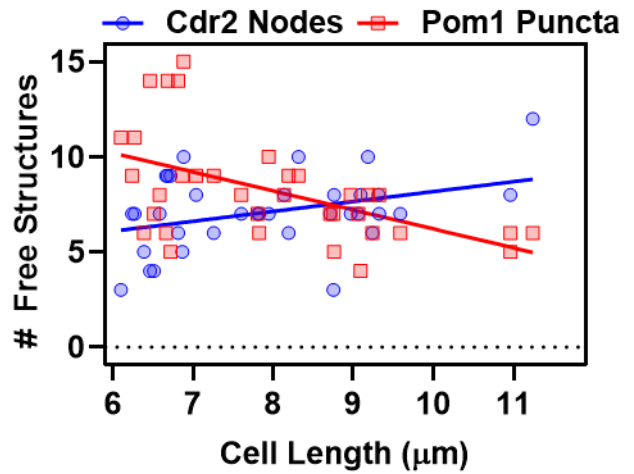
Medial Fluorescence (A.U.)



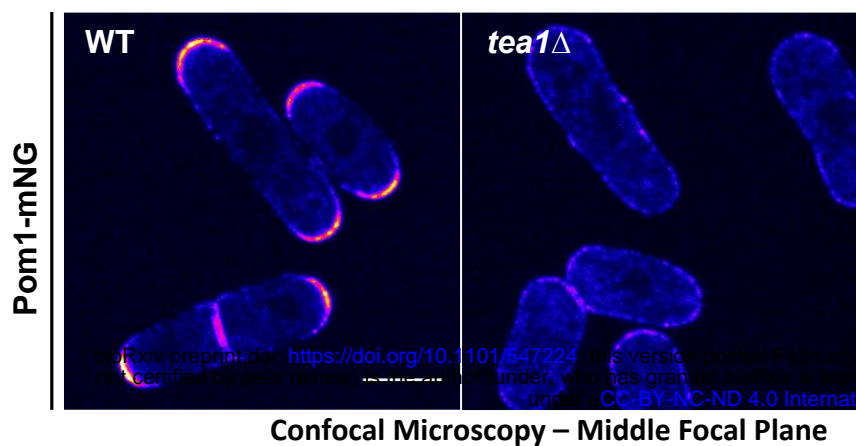
E.



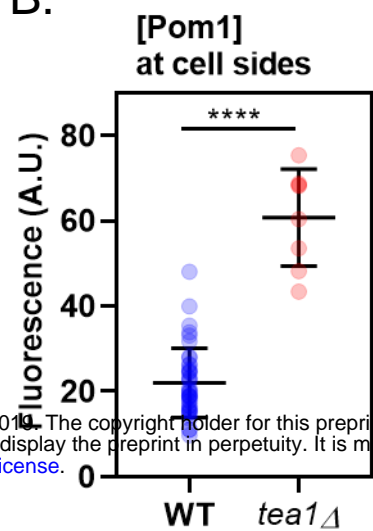
F.



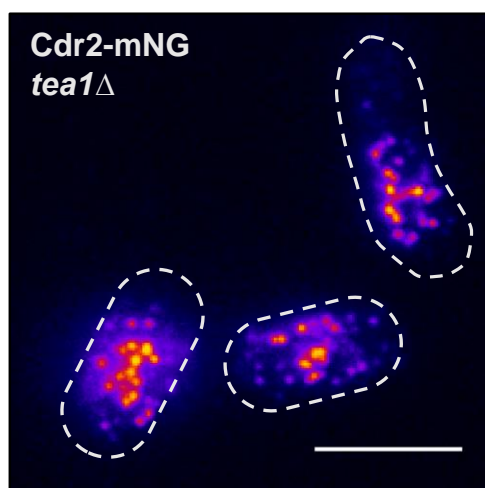
A.



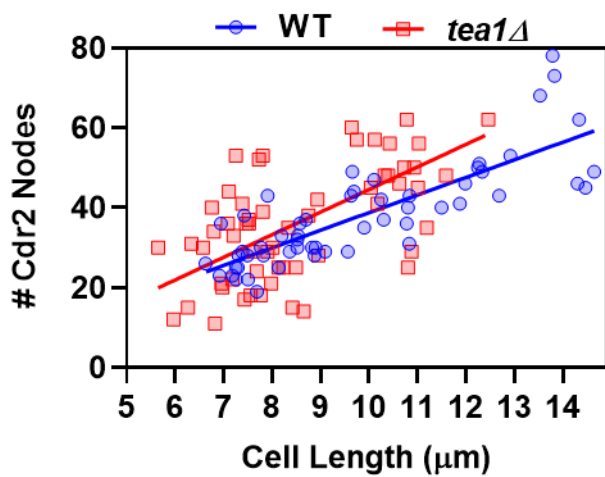
B.



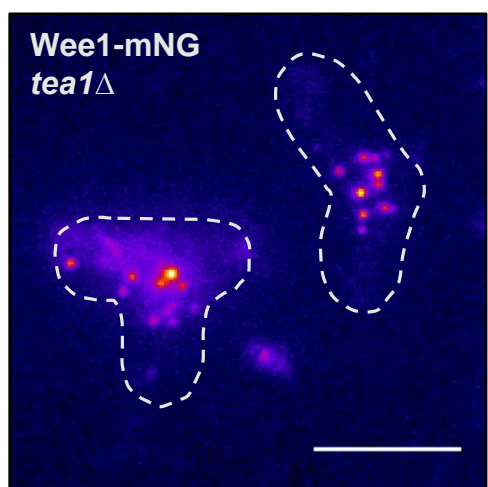
C.



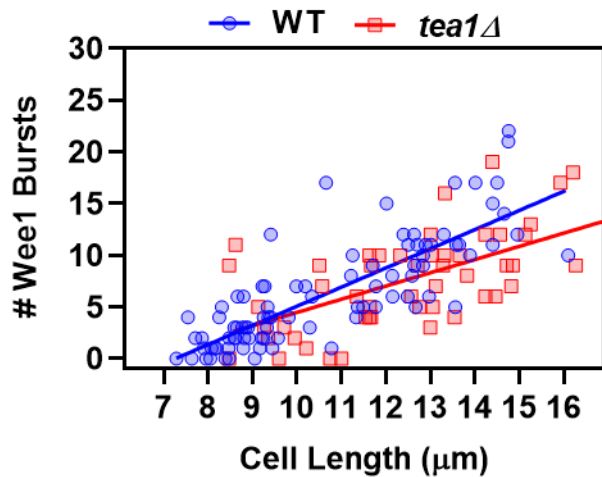
D.

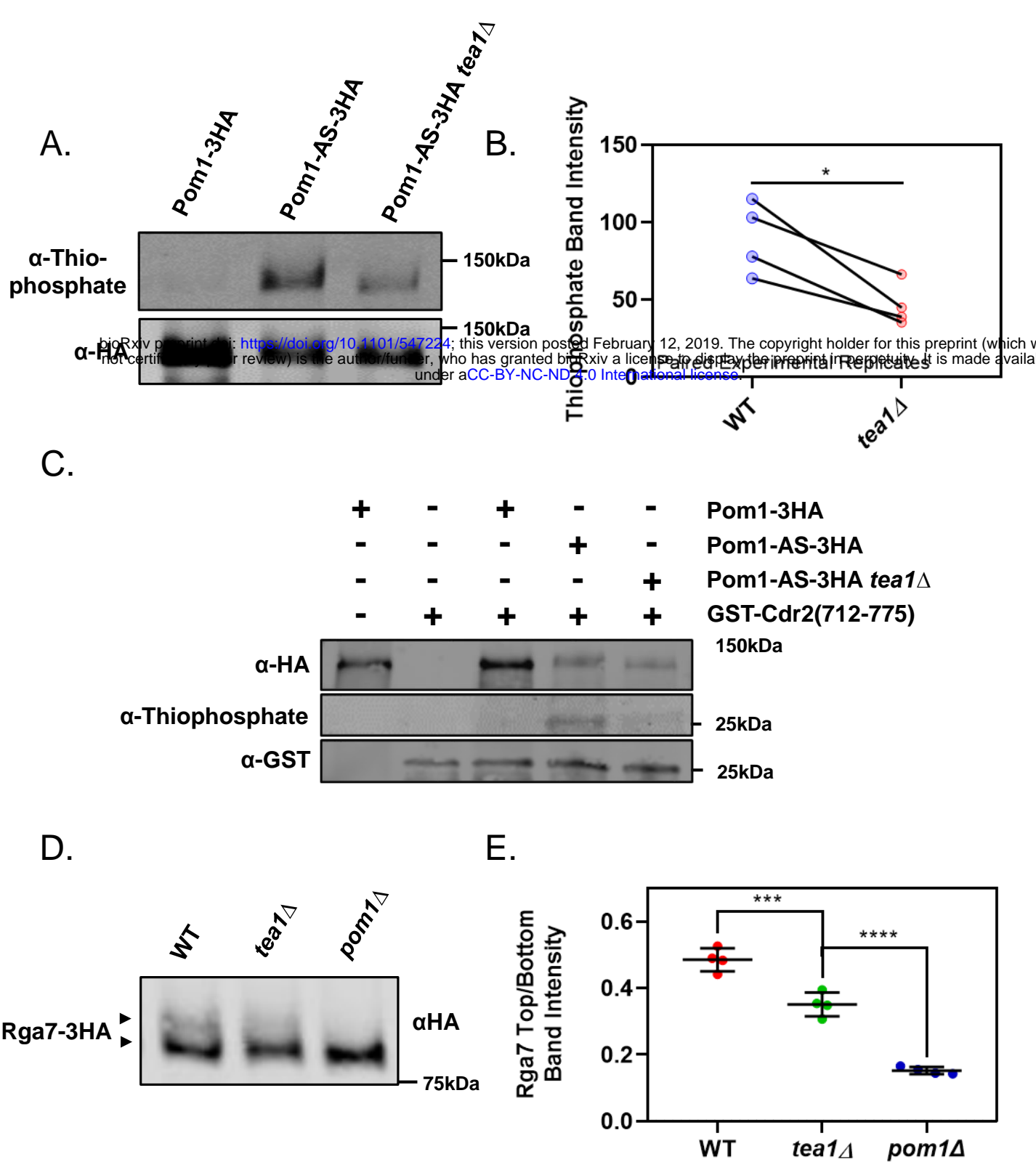


E.

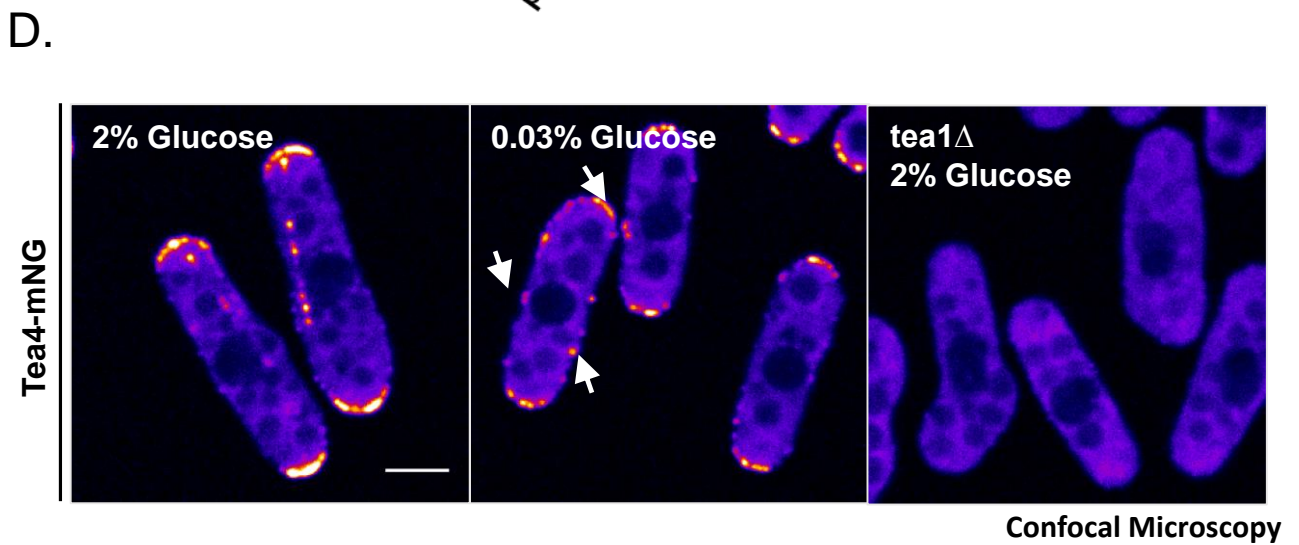
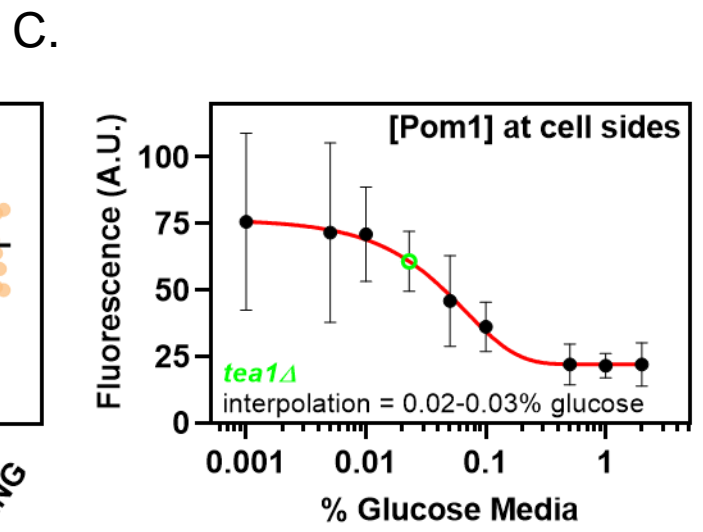
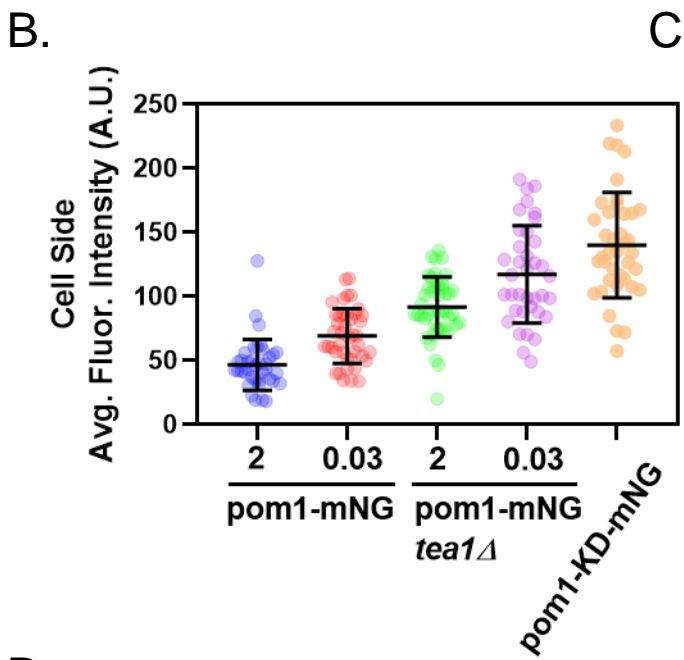
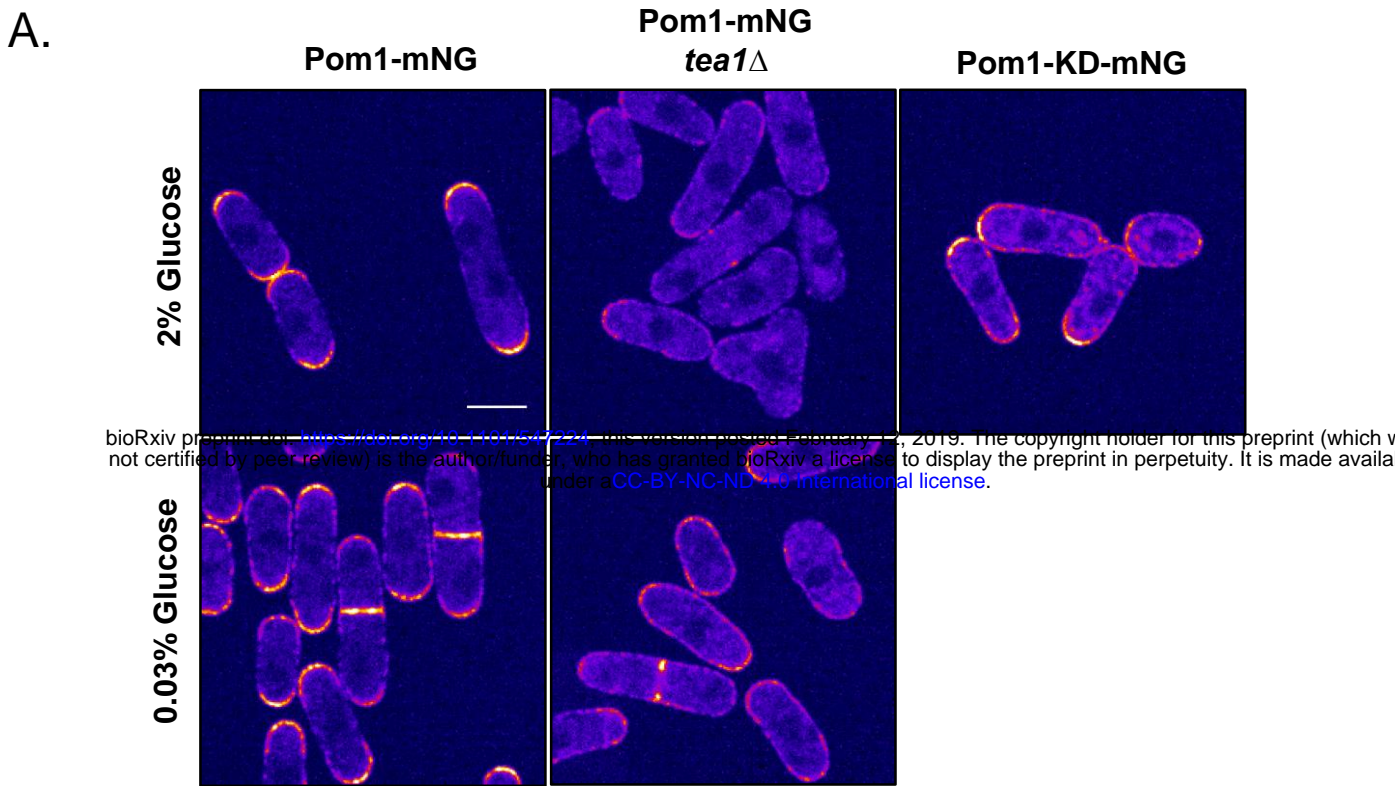


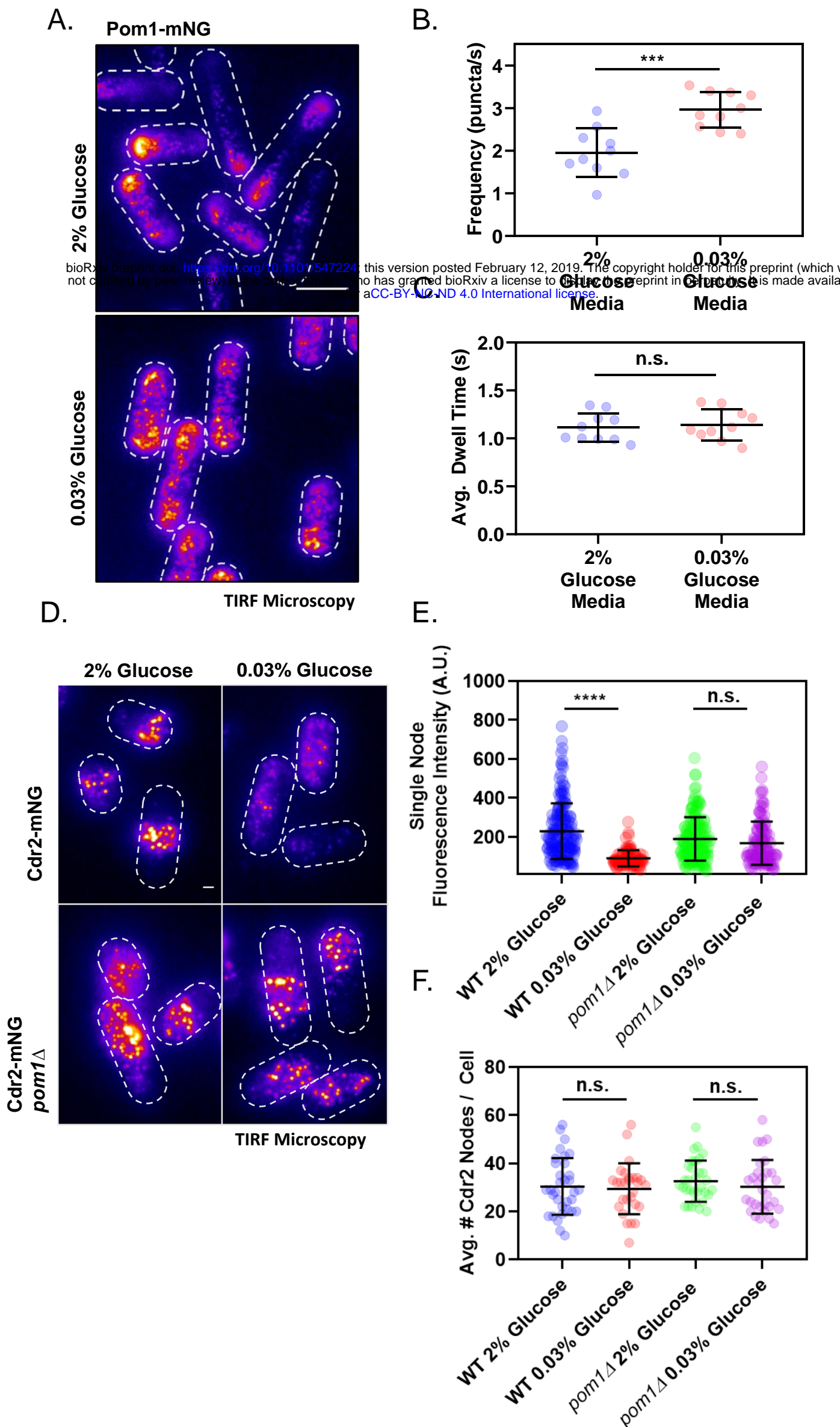
F.





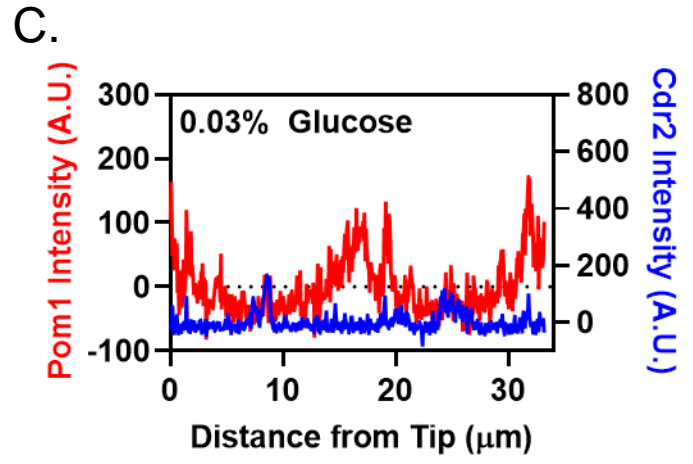
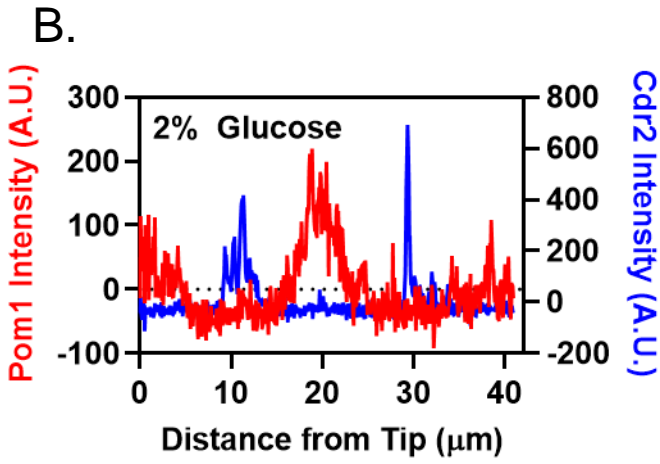
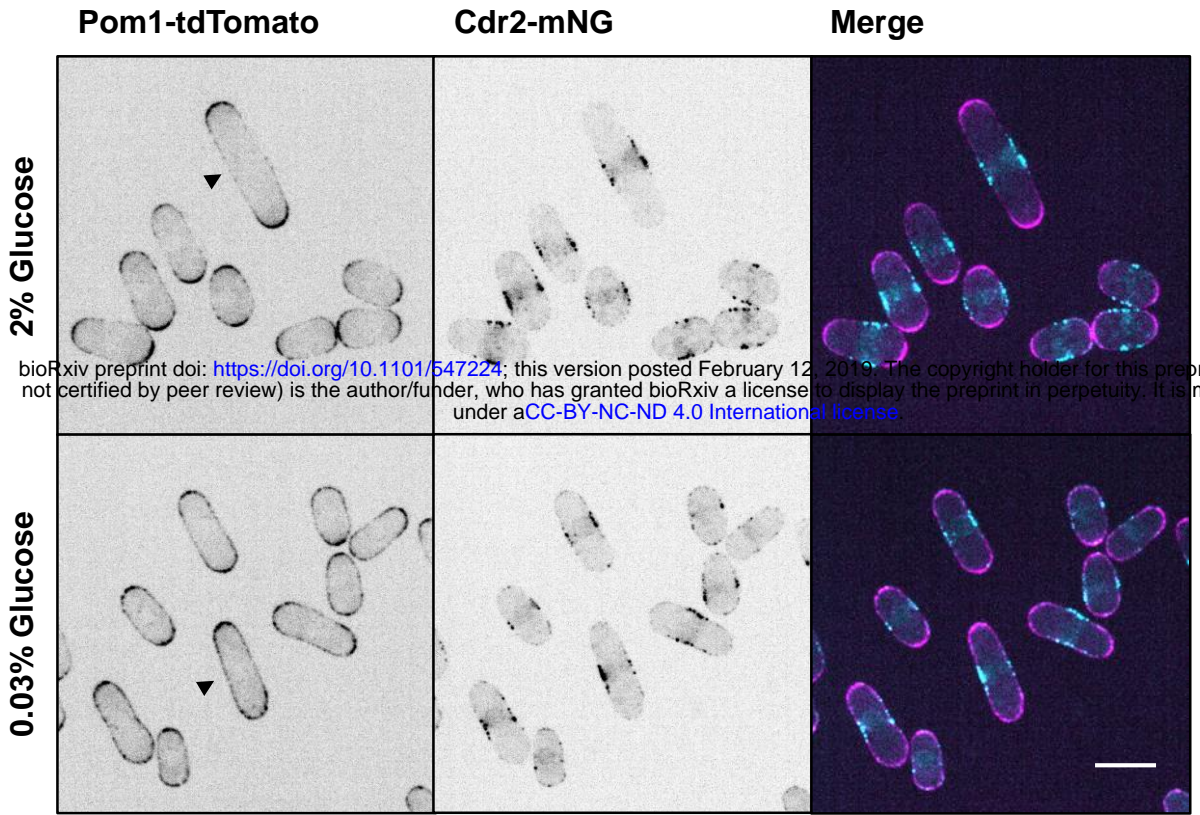
Supplemental Figure 5 in support of Figure 5





**Figure 6**

# A. Confocal Microscopy



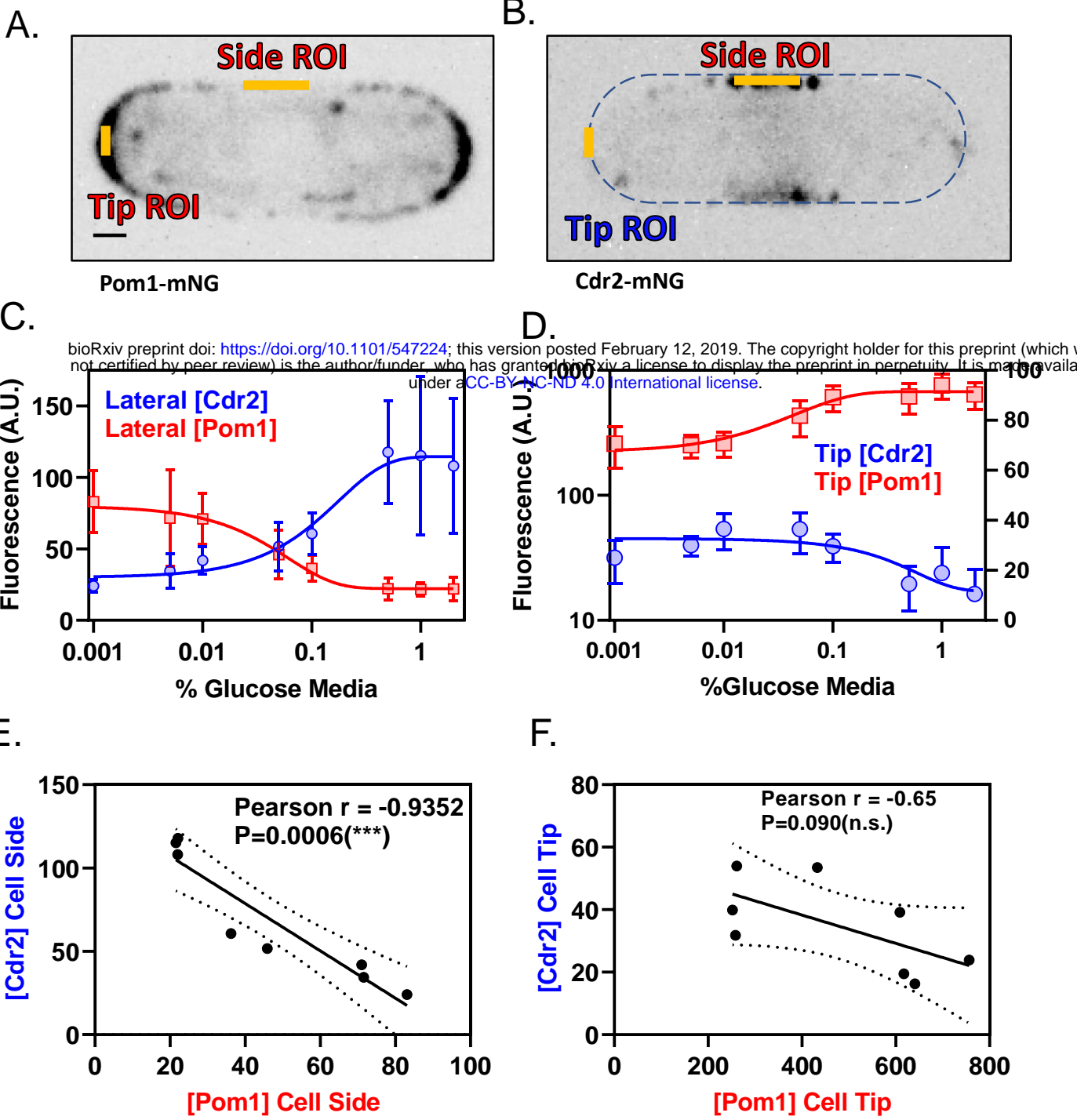
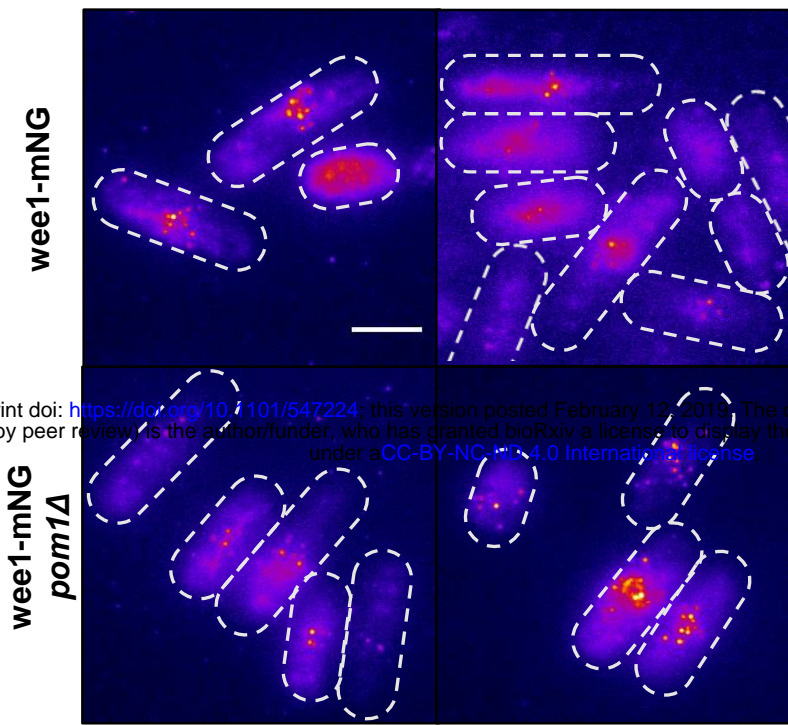


Figure 7

A.

2% Glucose

0.03% Glucose

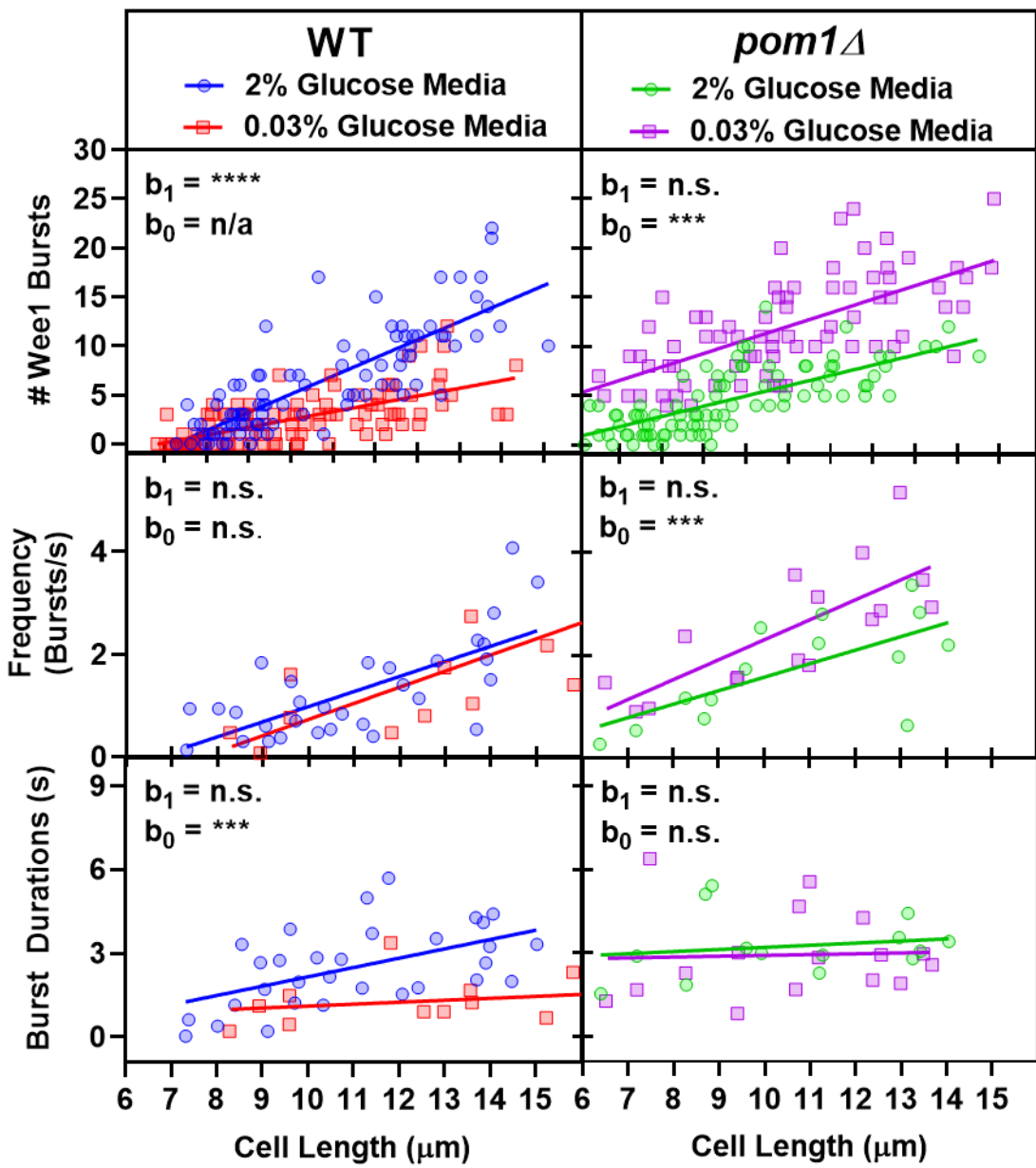


bioRxiv preprint doi: <https://doi.org/10.1101/547224>; this version posted February 12, 2019. The copyright holder for this preprint (which was not certified by peer review) is the author/funder, who has granted bioRxiv a license to display the preprint in perpetuity. It is made available under aCC-BY-NC-ND 4.0 International license.

TIRF Microscopy

B.

C.



D.

WT

*pom1*Δ*cdr2*Δ

2%

0.03%

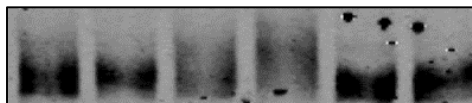
2%

0.03%

2%

0.03%

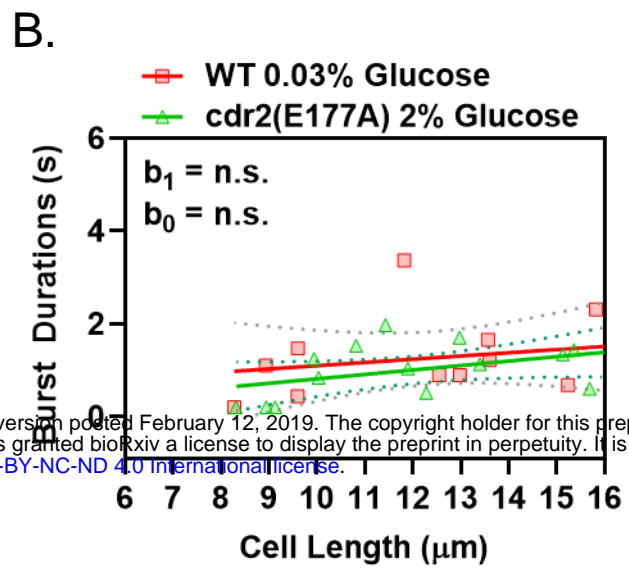
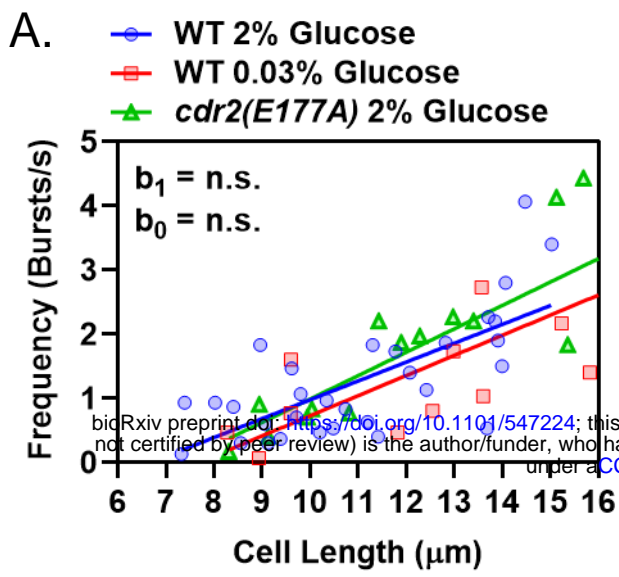
Glucose



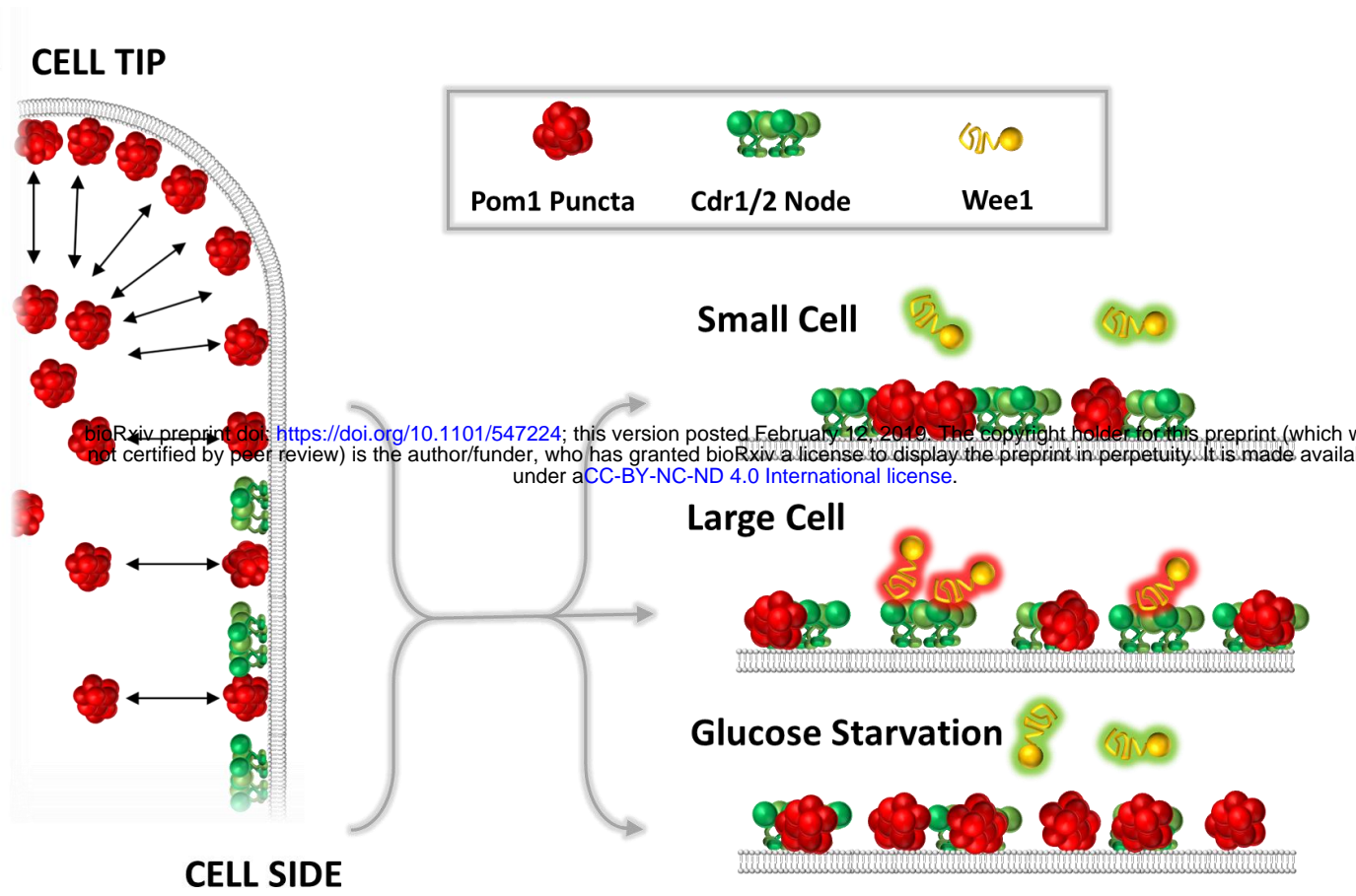
αWee1

Figure 8





bioRxiv preprint doi: <https://doi.org/10.1101/547224>; this version posted February 12, 2019. The copyright holder for this preprint (which was not certified by peer review) is the author/funder, who has granted bioRxiv a license to display the preprint in perpetuity. It is made available under aCC-BY-NC-ND 4.0 International license.



**Figure 9**

**Strains used in this study:**

Strain	Genotype	Origin	Figure
JM4496	<i>pom1-yomNeonGreen::hphR</i>	This Study	1A-I, S1A-K, 2A-B,E-F, S2A,D, 3D-F, S3A-B, 4C-E, S4A-D, 5A-B, S6A-C, 6A-C, 7A,C-F
JM797	<i>pom1-3HA::hphR ura4-D18 leu1-32 h+</i>	PN948 (Paul Nurse Lab)	2C-D,G, S5A,C
JM966	<i>pom1Δ::natR h-</i>	Lab Stock	2G, 8D
JM5412	<i>pom1-m2-yomNeonGreen::hphR ura4-D18 leu1-32 h-</i>	This Study	S2D, S6A-B
JM5414	<i>pom1-3HA::hphR tea1Δ::ura4+ ura4-D18</i>	This Study	3A
JM5415	<i>pom1-3HA::hphR tea4Δ::kanMX6</i>	This Study	3A
JM4792	<i>pom1-yomNeonGreen::hphR tea1Δ::kanMX6</i>	This Study	3B-F, S3A-B, 5A-B, S6A-C
JM4791	<i>pom1-yomNeonGreen::hphR tea4Δ::kanMX6</i>	This Study	3B-F, S3A-B
JM5373	<i>pom1-yomNeonGreen::hphR cdr2-tagRFP-t::hphR</i>	This Study	4A-B
JM4493	<i>cdr2-yomNeonGreen::hphR h-</i>	Lab Stock	4C-E, 6D-F, 7B-F
JM4525	<i>wee1-yomNeonGreen::hphR cdr2Δ::natR</i>	Lab Stock	S4A-C
JM5133	<i>hphR cdr2Δ::natR ura4-D18 leu1-32 h+</i>	This Study	S4A-C, S5A-F, S7A-F
JM5374	<i>hphR cdr2Δ::natR ura4-D18 leu1-32 h+</i>	This Study	S4A-C, S5A-F, S7A-F
JM5372	<i>wee1-yomNeonGreen::hphR tea1Δ::kanMX6</i>	This Study	S5D-E
JM2209	<i>rga7-3HA::hphR h-</i>	Lab Stock	S5D-E
JM5612	<i>rga7-3HA::hphR tea1Δ::kanMX6</i>	This Study	S5D-E
JM2210	<i>rga7-3HA::hphR pom1Δ::kanMX6</i>	Lab Stock	S5D-E
JM4211	<i>pom1-as-3HA::hphR</i>	Lab Stock	S5A-C
JM5565	<i>pom1-as-3HA::hphR tea1Δ::kanMX6 ura4-D18</i>	This Study	S5A-C
JM5132	<i>tea4-yomNeonGreen::hphR h-</i>	This Study	S6D
JM5733	<i>tea4-yomNeonGreen::hphR tea1Δ::kanMX6</i>	This Study	S6D
JM5359	<i>cdr2-yomNeonGreen::hphR pom1Δ::natR</i>	This Study	6D-F
JM4495	<i>wee1-yomNeonGreen::hphR h-</i>	Lab Stock	8A-B, S8A-B
JM4527	<i>wee1-yomNeonGreen::hphR pom1Δ::kanMX6</i>	Lab Stock	8A,C
JM366	972 <i>h-</i>	PN1 (Paul Nurse lab)	8D
JM600	<i>cdr2Δ::natR ura4-D18 leu1-32 h+</i>	Lab Stock	8D
JM4578	<i>wee1-yomNeonGreen::hphR cdr2(E177A)</i>	Lab Stock	S8A-B

bioRxiv preprint doi: <https://doi.org/10.1101/317224>; this version posted February 12, 2019. The copyright holder for this preprint (which was not certified by peer review) is the author/funder, who has granted bioRxiv a license to display the preprint in perpetuity. It is made available under aCC-BY-NC-ND 4.0 International license.